

**NOAA NESDIS
CENTER for SATELLITE APPLICATIONS and
RESEARCH**

ALGORITHM THEORETICAL BASIS DOCUMENT

**Overshooting Top and Enhanced-V
Detection**

Kristopher Bedka, SSAI @ NASA LaRC

Jason Brunner, UW/CIMSS

Wayne Feltz, UW/CIMSS

Version 1.0

June 7, 2011

TABLE OF CONTENTS

1	INTRODUCTION	9
1.1	Purpose of This Document.....	9
1.2	Who Should Use This Document	9
1.3	Inside Each Section.....	9
1.4	Related Documents	10
1.5	Revision History	10
2	OBSERVING SYSTEM OVERVIEW.....	10
2.1	Products Generated	10
2.2	Instrument Characteristics	11
3	ALGORITHM DESCRIPTION.....	12
3.1	Algorithm Overview	12
3.2	Processing Outline	13
3.3	Algorithm Input	16
3.3.1	Primary Sensor Data	16
3.3.2	Ancillary Data.....	16
3.3.3	Derived Data	16
3.4	Theoretical Description.....	16
3.4.1	Physics of the Problem.....	16
3.4.1.1	Objective Overshooting Top Detection	16
3.4.1.2	Objective Enhanced-V Signature Detection	24
3.5	Algorithm Output.....	29
4	TEST DATA SETS AND OUTPUTS.....	32
4.1	Simulated/Proxy Input Data Sets	32
4.2	Validation Truth Data Sets and Methodology	33
4.2.1	CloudSat OT Observations	33
4.2.2	WRF ARW Simulated OT Events	34
4.2.3	MODIS + AVHRR Enhanced-V and ATC Database	36
4.3	Output from Simulated/Proxy Input Data Sets	37
4.3.1	MODIS-Based Proxy ABI OT Detections and Comparison With CloudSat OT Observations	37
4.3.2	ARW-based Synthetic ABI OT Detections and Comparison With ARW THMR Output.....	44
4.3.3	MODIS + AVHRR Enhanced-V and ATC Database	47
5	PRACTICAL CONSIDERATIONS.....	50
5.1	Numerical Computation Considerations	50
5.2	Programming and Procedural Considerations	50
5.3	Quality Assessment and Diagnostics	50
5.4	Exception Handling	50
5.5	Algorithm Validation	50
6	ASSUMPTIONS AND LIMITATIONS	50
6.1	Performance	50
6.2	Assumed Sensor Performance	51
6.3	Pre-Planned Product Improvements	51
6.3.1	Improved OT Detection In Banded Cold Cirrus Cloud Cases.....	51

6.3.2 Inclusion of NWP 250 hPa Wind Direction	51
7 REFERENCES	52

LIST OF FIGURES

Figure 1 - High level flowchart of the OT detection algorithm illustrating the main processing sections.....	14
Figure 2 - High level flowchart of the enhanced-V ATC detection algorithm illustrating the main processing sections.....	15
Figure 3 - (left) NOAA AVHRR 1 km visible imagery at 2253 UTC on 11 June 2008 showing a line of severe convective storms across Minnesota, Iowa, Nebraska, and Kansas. Pixels detected by the 2 km ABI OT algorithm are shown in red. (right) A mosaic of WSR-88D composite reflectivity data at 2 km resolution over the same region. Comparison between the left and right panels shows that satellite OT detections correlate well with the most intense radar echoes.	19
Figure 4 – The frequency of turbulence from United Airlines Eddy Dissipation Rate observations when aircraft fly within varying distance from detected GOES-12 OTs (red) and cold pixels (IR temperature < 215 K) that do not meet the OT detection criteria (blue). Turbulence is observed significantly more often when aircraft fly very close to OTs.....	19
Figure 5 - (left) GOES-12 1 km visible channel imagery at 0045 UTC on 6 July 2005. OTs for one cluster of thunderstorm cells are highlighted by the red arrows, with the gravity waves induced by these OTs identified by orange arrows. Objective EDR turbulence observations of light (moderate) intensity are shown in blue (green). Null turbulence observations are shown in grey. (right) The corresponding color-enhanced GOES-12 4 km 10.7 μ m IR window channel imagery with EDR observations.	20
Figure 6 - (left column) Terra MODIS imagery at 1655 UTC on 8 June 2008, (top) Color enhanced IR window channel imagery with cool colors representing the colder cloud tops, (bottom) WV-IR BTD of +2 K (blue) and +4 K (cyan). (right column) The same imagery and products, but from Aqua MODIS at 1840 UTC on the same day.....	20
Figure 7 - (black line) The frequency of OT minimum IRW BTs less than BT values along the bottom x-axis scale for 450 enhanced-V producing thunderstorms described by Brunner et al. (2007). (grey line) The frequency of the OT minimum BT minus mean surrounding anvil BT less than BT difference values along the top x-axis scale for the same 450 thunderstorm database. Circles along the two lines represent criteria used in the IRW-texture OT detection method.	23
Figure 8 - A graphical example of the ABI overshooting top detection algorithm. (top-left) MODIS 250 m visible channel image at 2315 UTC on 5/9/2008. (top-right) MODIS 1 km IRW image at the same date and time. The center of a cluster of black lines indicates a pixel with an IRW BT less than or equal to 215 K and the NWP tropopause temperature that is not at least 6.5 K colder than the surrounding anvil. The end point of each of the black lines shows the 16 pixels that were included in the mean anvil BT calculation. The center of a cluster of white lines indicates a cold pixel that is also significantly colder than the surrounding anvil and is therefore considered an overshooting top pixel. (bottom) The final OT detection field (red pixels) after the remaining pixels that compose the OT are identified. The diagonal white line extending across the three images shows the location of a CloudSat overpass that will be discussed later.	23

Figure 9 - (left) An example of an enhanced-V signature present in 1 km AVHRR 10.8 μm IRW imagery on 9 July 2009 at 1133 UTC. The IRW imagery is superimposed atop visible channel imagery, giving the image a pseudo 3-D appearance. (right) Severe weather reports on 9 July 2009. The location of the storm shown in the left panel is indicated.....	25
Figure 10 - MODIS and AVHRR \sim 11 μm IR window imagery for 8 enhanced-V events. All images cover the same horizontal distance and use same color enhancement, illustrating the significant variations in the V-signature across events.....	25
Figure 11 – (left) GOES-12 and (right) MODIS 10.7 μm IRW imagery for a thunderstorm complex with several enhanced-V signatures.	26
Figure 12 - A schematic representation of the ABI ATC detection algorithm using MODIS IR window imagery degraded to the 2 km ABI IR resolution for an enhanced-V case in Tennessee. Labeled upon the graphic are the enhanced-V location (white dashed line), the downstream warm area search box (black), the OT minimum BT location (cyan), the downstream warm area location and maximum BT (green), and the ray extending 50 km beyond the warm area with end of ray BT (yellow)	28
Figure 13 - A cumulative frequency diagram of the distance between the manually identified minimum IR window channel OT and downstream warm area BT for the 450 enhanced-V cases described by Brunner et al. (2007).....	28
Figure 14- A cumulative frequency diagram of the manually identified downstream warm area maximum IR window channel BT for the 450 enhanced-V cases described by Brunner et al. (2007).....	29
Figure 15 - A cumulative frequency diagram of the difference between the OT minimum and downstream warm area maximum BT for the 450 enhanced-V cases described by Brunner et al. (2007).....	29
Figure 16 - (upper-left) A top view of the 0.05 g/kg THMR isosurface colored by simulated GOES-R ABI 11.2 μm IRW BTs. OTs appear as localized cold regions surrounded by a warmer anvil cloud. Warm temperatures for clear sky and low cloud pixels are transparent. (upper-right) A side view of the same isosurface showing that the two OTs have heights significantly higher than the anvil cloud. The isosurface is colored here by the ARW 3-D temperature field. ARW THMR output at 200 hPa (lower-left), 175 hPa (lower-middle), and 150 hPa (lower-right) showing that high THMR values are associated with the OTs identified in the top panels. Graphics were produced using the McIDAS-V visualization software developed at UW-SSEC.....	36
Figure 17 - (top) A CloudSat overpass of a deep convective cloud with an OT over the South Pacific on 9 May 2008 at 2317 UTC. The region within the two vertical dashed lines is the OT. The horizontal lines denote the peak height of the OT and the height of the anvil cloud surrounding the OT. (lower-left) Contrast-enhanced Aqua MODIS 0.25 km visible channel imagery at 2315 UTC. (lower-right) Color-enhanced Aqua MODIS 1 km IRW BT imagery. The white diagonal line in the bottom panels shows the location of the CloudSat overpass from the top panel.	39
Figure 18 - (top) A CloudSat overpass of a deep convective cloud with an OT over the South Pacific on 9 October 2008 at 1142 UTC. The region within the two vertical dashed lines is the OT. The horizontal lines denote the peak height of the OT and the height of the anvil cloud surrounding the OT. (lower-left) Contrast-enhanced Aqua MODIS 0.25 km visible channel imagery at 1140 UTC. (lower-right) Color-enhanced Aqua MODIS 1	

km IRW BT imagery. The white diagonal line in the bottom panels shows the location of the CloudSat overpass from the top panel. Note that the BT range of the color-enhancement of the lower-right panel differs from that of the corresponding panel in Figure 19 - ABI OT detections (red pixels) for the 9 May 2008 (left) and 9 October 2008 (right) cases shown in Figs. 17 and 18.....	41
Figure 20 - A map of the 114 OTs identified within CloudSat CPR observations from April 2008 to September 2009. Red circles indicate OTs that were accurately detected by the ABI IRW-texture method and green circles indicate those that were undetected.	41
Figure 21 - (top) A CloudSat overpass of a deep convective cloud with an OT over the Congo on 29 November 2008 at 1213 UTC. The region within the two vertical dashed lines is the OT. The horizontal lines denote the peak height of the OT and the height of the anvil cloud surrounding the OT. (bottom-left) Contrast-enhanced Aqua MODIS 0.25 km visible channel imagery at 1210 UTC. (bottom-right) Aqua MODIS 1 km IRW BT imagery. The white diagonal line in the bottom panels shows the location of the CloudSat overpass from the top panel.	43
Figure 22 - IRW-texture OT detections with (red pixels) and without (blue pixels) the use of a GDAS tropopause temperature check for the case shown in Figure 20. The OTs detected with the tropopause temperature check were also detected when this check was removed.....	43
Figure 23 - a) Synthetic GOES-R ABI 11.2 μm IRW channel imagery. The color enhancement matches that shown in Fig. 9. b) Truth OT pixels as defined by ARW THMR. OT pixels with cloud tops above the 175 hPa level are colored in grey, pixels with tops above the 165 hPa level are colored in black, and high confidence OT pixels are colored in green. c) IRW-texture OT detections d) WV-IRW BTD values between 2 and 3 K (purple) and greater than 3 K (cyan). All images correspond to the 2340 UTC timestep on 4 June 2005 of the ARW simulation. The cluster of high confidence OTs in northeast Oklahoma corresponds to the clouds shown in Figure 1.	46
Figure 24 - Enhanced-V ATC detections with color-enhanced proxy GOES-R ABI IR window channel imagery at 1845 UTC on 7 April 2006. Enhanced-V locations are outlined in black dashed lines. Blue symbols are OT detects and green symbols are associated downstream warm regions, which together form the ATC. Only OTs with ATCs are shown.....	48
Figure 25 – A gallery of four enhanced-V producing storms in AVHRR-based proxy ABI 10.8 μm IRW imagery with OT and ATC detection output. The case occurred on 10 May 2004 at 2315 UTC. Blue (Green) squares show OT (ATC) detections and the white dashed line highlights the location of the enhanced-V signature in each panel.	49

LIST OF TABLES

Table 1 - ABI channel numbers and wavelengths. The channel used in the OT and ATC algorithms is indicated in the right column.....	11
Table 2 - GOES-R Series Ground Segment (GS) Project Functional and Performance Specification (F&PS) for the overshooting top and enhanced-V detection products.....	12
Table 3 – A description of the overshooting top detection output from the ABI OT algorithm.....	30
Table 4 - A description of the anvil thermal couplet output from the ABI ATC algorithm.	30
Table 5 – A description of the quality assurance flag values for the ABI OT algorithm .	30
Table 6 – A description of the metadata for the ABI OT algorithm.....	31
Table 7 - A description of the quality assurance flag values for the ABI ATC algorithm	31
Table 8 - A description of the metadata for the ABI ATC algorithm.....	31
Table 9 – A description of additional quality control parameters included in OT and ATC algorithm AIT FRAMEWORK output.	32
Table 10 – Validation statistics for the IRW-texture ABI OT detection algorithm with and without the use of NWP tropopause temperature information relative to statistics for the WV-IRW BTD method.....	42
Table 11 - Results from a statistical comparison between OTs detected in synthetic ABI IRW channel imagery, WV-IRW BT difference imagery, and truth OT locations defined by ARW THMR. Results for the baseline ABI OT detection algorithm settings are highlighted in bold text.	47
Table 12 - Validation statistics for the ABI enhanced-V ATC detection algorithm.	49

LIST OF ACRONYMS

ABI - Advanced Baseline Imager
AIT - Algorithm Integration Team
ARW – Advanced Research WRF NWP model
ATBD - Algorithm Theoretical Basis Document
ATC – Anvil Thermal Couplet
AVHRR - Advanced Very High Resolution Radiometer
AWG - Algorithm Working Group
BT – Brightness Temperature
BTD – Brightness Temperature Difference
CIMSS - Cooperative Institute for Meteorological Satellite Studies
CLASS – Comprehensive Large Array Stewardship System
CONUS – Continental U.S.
DPC – Data Processing Center
F&PS - Functional and Performance Specification
FAR – False Alarm Ratio
FRAMEWORK – NOAA/NESDIS/STAR GOES-R AIT processing framework
GDAS – Global Data Assimilation System
GFS - Global Forecast System
GOES - Geostationary Operational Environmental Satellite
GS – Ground System
ID - Identification
IRW – IR Window
LaRC – Langley Research Center
LAADS – NASA MODIS Level 1 and Atmosphere Archive and Distribution System
MODIS - Moderate Resolution Imaging Spectroradiometer
MSG - Meteosat Second Generation
NAM – North American Mesoscale Model
NASA - National Aeronautics and Space Administration
NESDIS - National Environmental Satellite, Data, and Information Service
NOAA - National Oceanic and Atmospheric Administration
NWP - Numerical Weather Prediction
OT – Overshooting Top
POD – Probability of Detection
QA – Quality Assurance
SEVIRI - Spinning Enhanced Visible and Infrared Imager
SSAI – Science Systems and Applications, Inc.
STAR - Center for Satellite Applications and Research
THMR – Total Hydrometeor Mixing Ratio
UW – University of Wisconsin
WRF – Weather Research and Forecasting model
WV – Water Vapor

ABSTRACT

This document provides a high level description of and the physical basis for the detection of overshooting convective cloud tops and anvil thermal couplets associated with the enhanced-V signature using images taken by the Advanced Baseline Imager (ABI) flown on the GOES-R series of NOAA geostationary meteorological satellites. This document will describe the required inputs, the theoretical foundation of the algorithms, the sources and magnitudes of the errors involved, practical considerations for implementation, and the assumptions and limitations associated with the product and provide a high level description of the physical basis for the detection of the overshooting top and enhanced-V signatures. Examples of product outputs and detailed results from product validation studies are also included.

1 INTRODUCTION

1.1 Purpose of This Document

The following algorithm theoretical basis document (ATBD) provides a high level description of and the physical basis for the detection of overshooting convective cloud tops and anvil thermal couplets associated with the enhanced-V signature using images taken by the Advanced Baseline Imager (ABI) flown on the GOES-R series of NOAA geostationary meteorological satellites. This document will describe the required inputs, the theoretical foundation of the algorithms, the sources and magnitudes of the errors involved, practical considerations for implementation, and the assumptions and limitations associated with the product and provide a high level description of the physical basis for the detection of the overshooting top and enhanced-V signatures.

1.2 Who Should Use This Document

The intended users of this document are those interested in understanding the physical basis of the algorithms and how to use the output of this algorithm to determine locations of hazardous weather often found in conjunction with overshooting tops and the enhanced-V signature. This document also provides information useful to anyone maintaining or modifying the original algorithm.

1.3 Inside Each Section

This document is broken down into the following main sections.

- **System Overview:** Provides relevant details of the ABI and provides a brief description of the products generated by the algorithm.

- **Algorithm Description:** Provides all the detailed description of the algorithm including its physical basis, its input and its output.
- **Assumptions and Limitations:** Provides an overview of the current limitations of the approach and gives the plan for overcoming these limitations with further algorithm development.

1.4 Related Documents

This document currently does not relate to any other document outside of the specifications of the GOES-R F&PS and to the references given through out.

1.5 Revision History

Version 0.1 of this document was created by Kristopher Bedka in September 2008 prior to the version 1.0 software delivery. This document has been revised following the document guideline provided by the GOES-R Algorithm Application Group (AWG). Version 1.0 of the document provides a thorough description of the current and future state of the algorithm as the structure of the code has advanced considerably in the time between pre-version 1.0 ATBD and the current version 3.0 software delivery.

2 OBSERVING SYSTEM OVERVIEW

This section describes the products generated by the ABI overshooting top and enhanced-V signature detection algorithms and the requirements they place on the sensor. *For the remainder of this document, anvil thermal couplet detection is synonymous with enhanced-V detection.*

2.1 Products Generated

Binary overshooting top (OT) and enhanced-V signature detection masks are the required products from this algorithm. The OT detection algorithm is responsible for identification of the active updraft region within strong convective storms. These pixels are used as input to the enhanced-V detection algorithm. As will be described later, detection of the enhanced-V signature itself is a significant challenge that is prone to false alarm. *The emphasis is directed toward detection of “anvil thermal couplets” (ATCs) that are regularly present within the cirrus anvil cloud of enhanced-V producing storms.* The ATC detection algorithm is responsible for identifying the presence of a warm area “downstream” (relative the anvil level wind flow) of an OT. A binary detection mask is generated to identify the locations of ATC pixels.

Though the binary OT and ATC detection masks are the official product requirements, several other ancillary products are produced to aid in product interpretation and quality control. For the OT algorithm, each OT is assigned an identification (ID) number so it can be matched with the corresponding ATC. The number of pixels used to compute the

mean temperature of the anvil cloud surrounding the OT is also output. This number ranges from 5 to 16 pixels and a more accurate OT detection mask is produced when a greater number of pixels is included in the mean (Bedka et al. 2010). The brightness temperature (BT) difference between the OT and surrounding anvil is also output, since a larger difference has also been shown by Bedka et al. to produce a more accurate OT detection mask. The minimum OT BT is also recorded because the occurrences of severe weather, lightning, and aviation turbulence have been shown to increase with decreasing BT. For the ATC detection algorithm, the OT ID number is assigned to the corresponding ATC detection so a user can determine which OT matches with which ATC. The BT difference between the OT and the ATC is preserved because large differences have been shown to be a strong indicator of severe weather (winds, hail, and/or tornadoes) at the surface (Brunner et al. 2007).

2.2 Instrument Characteristics

The OT and ATC detection algorithms utilize only the ABI 11.2 μm channel (i.e. Channel 14). Though no current satellites have a 10.35 μm channel (i.e. Channel 13), we believe that data from the 10.35 μm channel could be utilized within these algorithms and produce little degradation in performance if the 11.2 μm channel were to fail.

The GOES-R Series Ground Segment (GS) Project Functional and Performance Specification (F&PS) states that product accuracy requirements for the OT and enhanced-V signature detection products must have a 1 – false alarm ratio (FAR) value of at least 75% for these algorithm outputs. See Table 2 for a full list of F&PS requirements.

<i>Channel Number</i>	<i>Wavelength (mm)</i>	<i>Used in OT and ATC Detection</i>
1	0.47	
2	0.64	
3	0.86	
4	1.38	
5	1.61	
6	2.26	
7	3.9	
8	6.15	
9	7.0	
10	7.4	
11	8.5	
12	9.7	
13	10.35	
14	11.2	✓
15	12.3	
16	13.3	

Table 1 - ABI channel numbers and wavelengths. The channel used in the OT and ATC algorithms is indicated in the right column.

Product Statistics Qualifier	Cloud Cover Conditions Qualifier	Product Extent Qualifier	Temporal Coverage Qualifiers	Product Measurement Precision	Vendor Allocated Ground Latency	Product Refresh Rate / Coverage Time	Measurement Accuracy	Measurement Range	Mapping Accuracy	Horizontal Resolution	Vertical Resolution	Geographic Coverage (G, H, C, M)	User & Priority	Name
Overshooting Top & Enhanced-V Detection	GOES-R Option 2	C,M	N/A	2 km	1 km	0-1 Binary (160-270 K)	25% (Defined by 1 minus False Alarm Ratio)	5 min	159 sec	5%	Day and Night	Quantitative out to at least 70% LZA and qualitative beyond	Clear conditions down to feature of interest with threshold accuracy	Over enhanced-V and overshooting top cases

Table 2 - GOES-R Series Ground Segment (GS) Project Functional and Performance Specification (F&PS) for the overshooting top and enhanced-V detection products.

3 ALGORITHM DESCRIPTION

3.1 Algorithm Overview

The OT and ATC algorithms are classified as “Option 2” algorithms within the GOES-R GS F&PS document. The OT and ATC are low-level algorithms that determine if overshooting convective cloud tops and a significant anvil thermal couplet are present at all ABI pixels within an image. The algorithms are required to process data from ABI CONUS and Mesoscale scans. These algorithms use the following to determine if each pixel represents an OT or ATC:

- 11.2 μm IR Window (IRW) Channel BT Imagery
- GFS NWP Model Tropopause Temperature

The OT and ATC algorithms derive the following ABI products listed in the F&PS:

- Binary OT detection mask
- Binary enhanced-V signature (i.e. ATC) mask

In addition, these algorithms derive the following products that are not included in F&PS.

- OT ID number
- Number of pixels used in computation of mean BT for the anvil cloud surrounding the OT

- Minimum 11.2 μm BT within the OT
- BT difference between the OT minimum BT and mean surrounding anvil BT
- Binary flag to indicate that an OT has an ATC
- ATC ID number recorded at the ATC mask locations which matches that of its parent OT ID number
- BT difference between the OT minimum BT and the ATC BT

3.2 Processing Outline

The processing outline of the OT and ATC detection algorithms are summarized in Figures 1 and 2. The current OT and ATC algorithms are implemented within the NOAA/NESDIS/STAR GOES-R AIT framework (FRAMEWORK). FRAMEWORK routines are used to provide all of the necessary ABI observations and ancillary data.

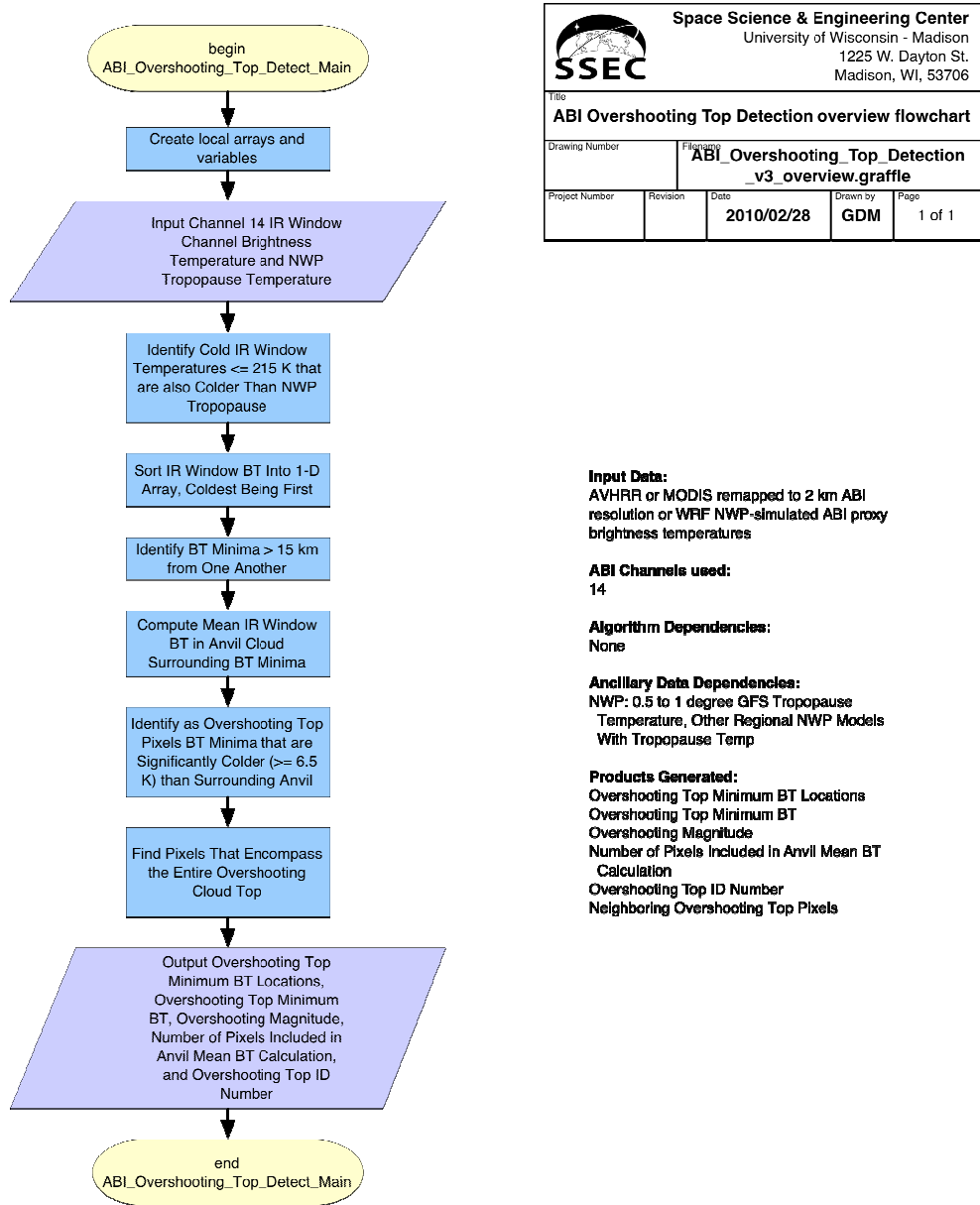


Figure 1 - High level flowchart of the OT detection algorithm illustrating the main processing sections.

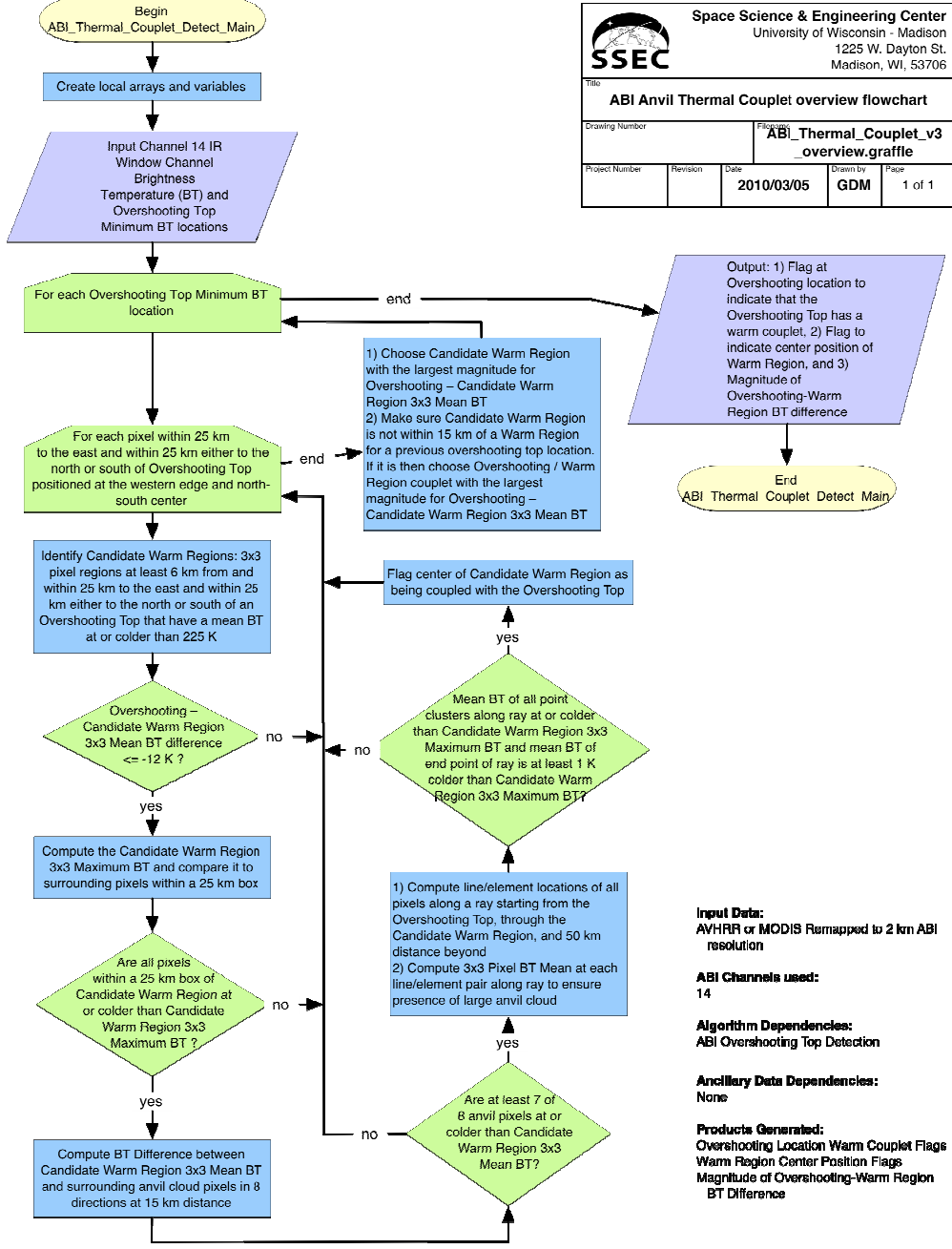


Figure 2 - High level flowchart of the enhanced-V ATC detection algorithm illustrating the main processing sections.

3.3 Algorithm Input

This section describes the inputs needed to process the OT and ATC algorithms. These algorithms must be run on arrays of pixels because spatial sampling of the convective cloud is an essential component of the algorithm processing. At the current time, the FRAMEWORK is unable to process overlapping scan segments. Thus the entire image must be read in and processed all at once.

3.3.1 Primary Sensor Data

The list below contains the primary sensor data used by the OT and ATC algorithm package. By primary sensor data, we mean information that is derived solely from the ABI observations and geolocation information.

- Calibrated BTs for ABI channel 14
- Sensor viewing zenith angle

3.3.2 Ancillary Data

The following data lists and briefly describes the ancillary data required to run the OT and ATC algorithms. By ancillary data, we mean required data that is not directly provided by the ABI observations or geolocation data.

- **Numerical Weather Prediction (NWP) Tropopause Temperature**
To ensure that a cloud is indeed “overshooting” the tropopause, the ABI channel 14 is compared against a NWP tropopause temperature analysis (or forecast for operational processing). If a pixel is at or colder than the tropopause, then it is considered for further processing by the OT detection algorithm. Currently the GFS is being used for this purpose.

3.3.3 Derived Data

No data from other ABI algorithms are required by the OT and ATC algorithms.

3.4 Theoretical Description

3.4.1 Physics of the Problem

3.4.1.1 Objective Overshooting Top Detection

OT detection is the process of identifying the portion of a convective cloud top that penetrates through the tropopause and into the stratosphere. OTs are important indicators of storm intensity, where the most intense radar reflectivity echoes are well correlated

with OTs observed by satellite imagery (see Figure 3). OTs are also a significant aviation turbulence hazard, as a deep layer of strong vertical motions are required to penetrate the statically stable tropopause region (see Figure 4). Horizontally and vertically propagating gravity waves are generated as the overshooting cloud tops interact with the tropopause region, which can produce turbulence for aviation far from the OT (see Figure 5). Bedka et al. (2010) also show a maximum in cloud-to-ground lightning activity near to the OT region.

OTs have the following unique characteristics in IR and Visible/Near-IR satellite imagery:

Visible/Near-Infrared Characteristics

- 1) “Lumpy” texture relative to smooth anvil cloud and shadowing at higher solar zenith angles
- 2) Variability in ice crystal effective radius and ~4 μm channel reflectance, with smaller ice crystals and higher reflectance indicating a severe storm (Rosenfeld et al. 2008)

Infrared-only Characteristics

- 1) Positive upper-level water vapor (WV) channel minus IRW channel BT differences (WV-IRW BTD) because anomalously high tropospheric water vapor content is injected into the lower stratosphere by OTs
- 2) Isolated region of very cold IR window channel BT relative to the surrounding warmer anvil cloud. Anomalously cold BTs are caused by persistent moist adiabatic ascent, allowing the BT to be much colder than any temperature found in a co-located sounding or NWP model temperature profile

Berendes et al. (2008) has shown that a combination of Visible + IR channel imagery can be effective within an unsupervised cloud classification technique for objective detection of deep convection and OTs. An extensive evaluation of this algorithm output for a variety of deep convection cases shows a significant diurnal signal in the classifier output, with a marked increase in the number of pixels classified as deep convection during the early morning and evening hours. This increase is caused by enhanced texture and cloud shadowing atop deep convective clouds at high solar zenith angles, which produces a significant increase in false OT detects. Near-IR effective radius and reflectance computations suffer from some of the same issues, making this technique unreliable for day/night OT detection. As the ABI OT algorithm is required to operate effectively during both day and night, the ABI Aviation AWG algorithm developers have concluded that the infrared only OT characteristics described above will be more reliable for satisfying the product requirements.

The WV-IRW BTD technique for OT detection has been described extensively in the literature (Fritz and Laszlo, 1993; Ackerman, 1996; Schmetz et al., 1997; Setvak et al., 2007). The WV-IRW technique is also known as the Global Convective Diagnostic and this product is currently operational at the NOAA National Weather Service Aviation Weather Center (Mosher, 2001). The premise behind this technique is that: 1) the

atmospheric temperature profile warms with height in the lower stratosphere, 2) WV is forced into the lower stratosphere at levels above the physical cloud top by the overshooting storm updraft, 3) this WV emits at the warmer stratospheric temperature, whereas the emission in the IRW channel originates from the colder physical cloud top, 4) positive differences between the warmer WV and colder IRW channel BTs can therefore identify where overshooting is occurring.

Setvak et al. (2007) provide the most comprehensive application of this method for OT detection using AVHRR, MODIS, MSG SEVIRI, and GOES imagery. Their results indicate that the required WV-IRW BTD threshold for OT detection can vary depending upon instrument spatial resolution, intensity of the convective updraft, and WV residence time in the stratosphere. In addition, the maximum WV-IRW BTD can be offset from the overshooting top location due to advection of stratospheric WV away from the emission source in the OT regions. Through comparison of positive Meteosat-8 WV-IRW BTD pixels with CloudSat cloud radar measurements, Chung et al. (2008) found that these pixels generally correspond with deep convective clouds whose tops were between 14 and 19 km. Vertical cloud depth of at least 4 km but often greater than 10 km were also observed for these pixels. Chung et al. also found a closer linear relationship between IRW BT and the WV-IRW BTD magnitude than between cloud depth and the BTD magnitude, indicating that high cloud top heights (and thus IRW BT) are a prerequisite for positive BTD.

Figure 6 shows that a WV-IRW BTD threshold of +2 K identifies a large portion of the anvil cloud as overshooting at both image times. The +4 K threshold at 1655 UTC occupies far too large an area to only be associated with overshooting tops. The coverage of +4 K at 1845 UTC appears more realistic. Though the differences in BTD results between the two image times could arise from differences in sensor calibration for Terra and Aqua, this example and those from Bedka et al. (2010) and Bedka (2010) indicate that no single WV-IRW BTD threshold provides consistently accurate OT detections.

One characteristic of OTs that has yet to be utilized in a published objective detection method is the fact that these features appear as small clusters of very cold pixels relative to the surrounding thunderstorm anvil. Spatial IRW BT gradients can be combined with NWP-based tropopause temperature information and knowledge of the characteristic size of an OT to objectively identify them at their proper spatial scale. Such a technique would have some advantages over the WV-IRW BTD in that: 2) it does not over-diagnose the size of OT regions, 2) it is not explicitly affected by the spatial/vertical distribution of atmospheric water vapor, , and 3) it does not use WV BT information which can be affected by variation in the central wavelength and/or spectral coverage of the WV absorption channel. The GOES-R ABI OT detection algorithm is based on this premise and the details of this algorithm are provided in the following section.

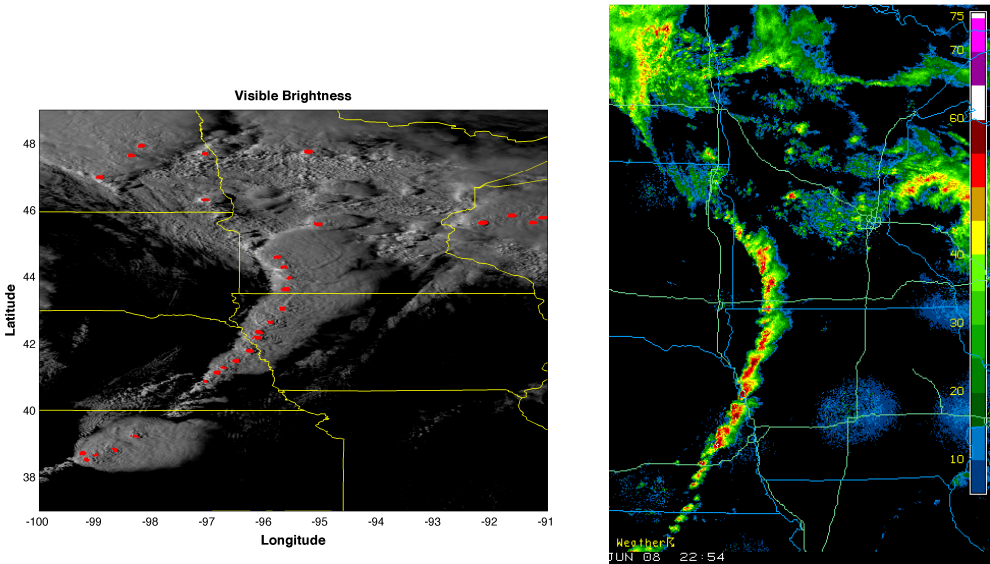


Figure 3 - (left) NOAA AVHRR 1 km visible imagery at 2253 UTC on 11 June 2008 showing a line of severe convective storms across Minnesota, Iowa, Nebraska, and Kansas. Pixels detected by the 2 km ABI OT algorithm are shown in red. (right) A mosaic of WSR-88D composite reflectivity data at 2 km resolution over the same region. Comparison between the left and right panels shows that satellite OT detections correlate well with the most intense radar echoes.

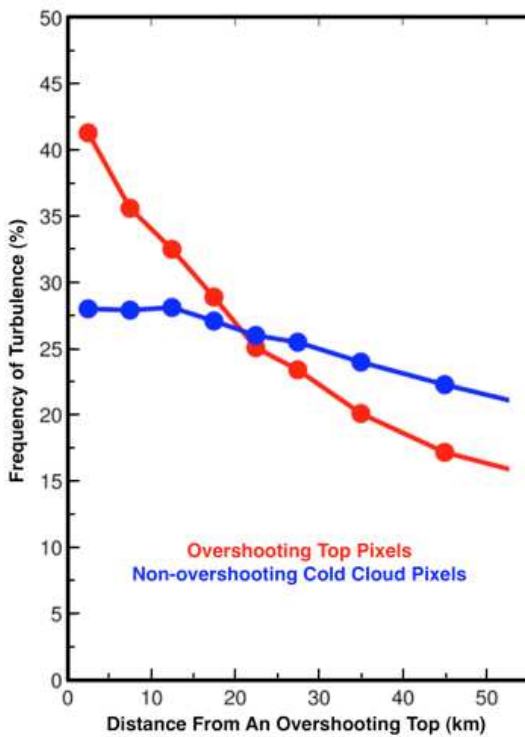


Figure 4 – The frequency of turbulence from United Airlines Eddy Dissipation Rate observations when aircraft fly within varying distance from detected GOES-12 OTs (red) and cold pixels (IR temperature < 215 K) that do not meet the OT detection criteria (blue). Turbulence is observed significantly more often when aircraft fly very close to OTs.

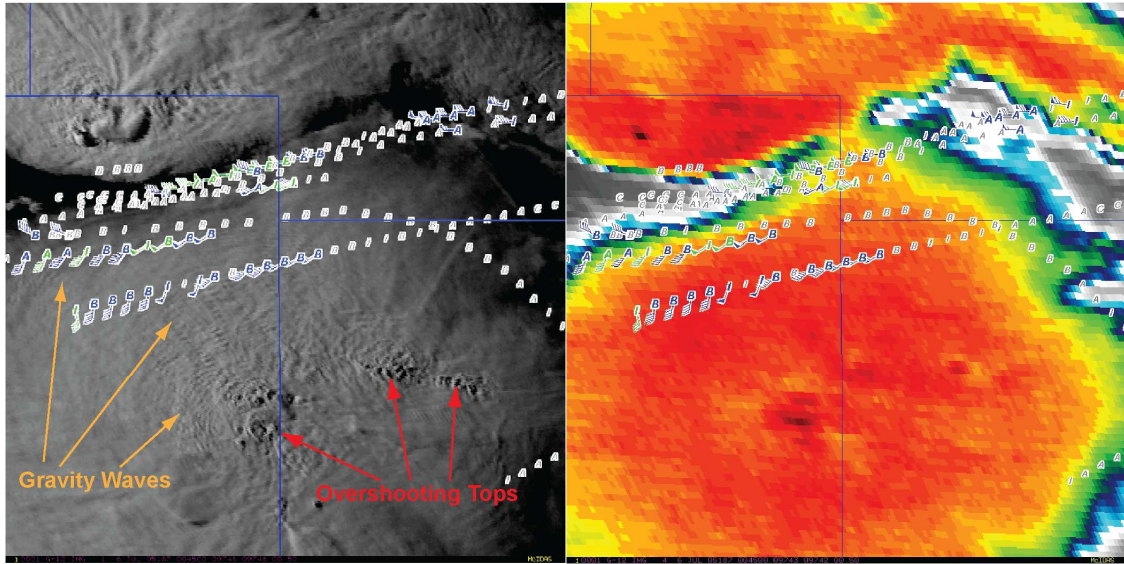


Figure 5 - (left) GOES-12 1 km visible channel imagery at 0045 UTC on 6 July 2005. OTs for one cluster of thunderstorm cells are highlighted by the red arrows, with the gravity waves induced by these OTs identified by orange arrows. Objective EDR turbulence observations of light (moderate) intensity are shown in blue (green). Null turbulence observations are shown in grey. (right) The corresponding color-enhanced GOES-12 4 km 10.7 μm IR window channel imagery with EDR observations.

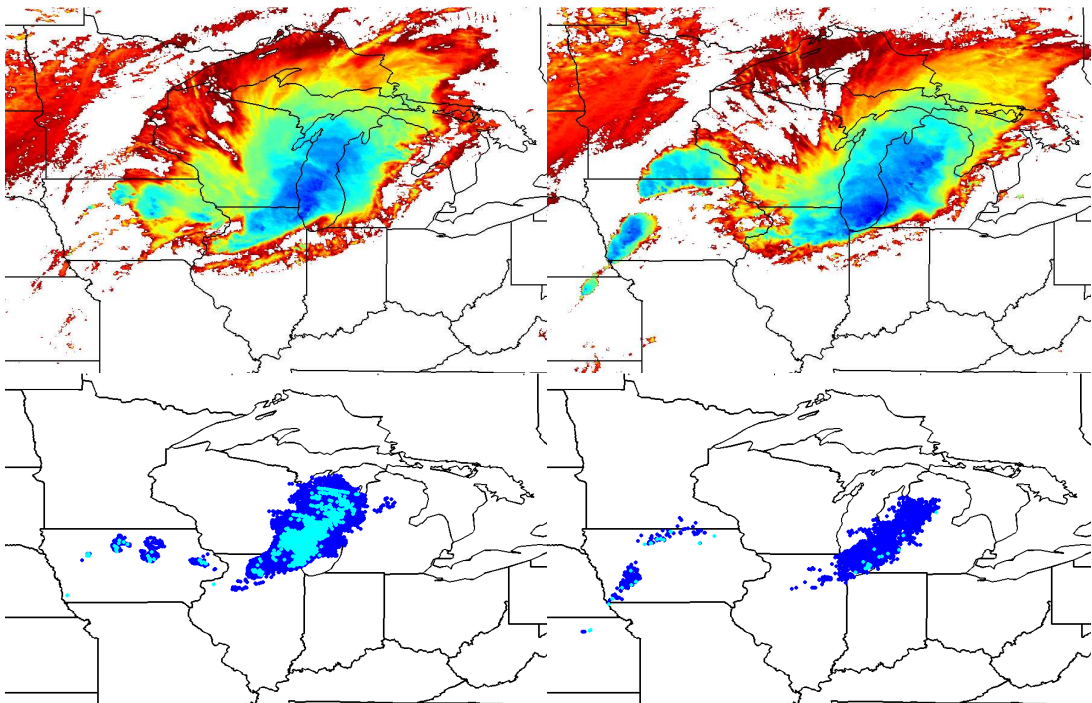


Figure 6 - (left column) Terra MODIS imagery at 1655 UTC on 8 June 2008, (top) Color enhanced IR window channel imagery with cool colors representing the colder cloud tops, (bottom) WV-IR BTD of +2 K (blue) and +4 K (cyan). (right column) The same imagery and products, but from Aqua MODIS at 1840 UTC on the same day.

3.4.1.1.1 The IRW-Texture ABI OT Detection Method

The premise behind the ABI OT detection algorithm is that OTs are isolated areas of very cold IR BT surrounded by a warmer anvil cloud. Brunner et al. (2007) has identified 450 enhanced-V producing storms during the 2003 and 2004 convective weather seasons in their development of a MODIS and AVHRR-based enhanced-V climatology over the CONUS. Figure 7 shows a cumulative frequency diagram of the minimum $\sim 11 \mu\text{m}$ IRW channel BT in regions subjectively identified as OTs for these 450 storms. Use of a 220 K brightness temperature threshold would have identified 100%, 215 K would have identified 95%, and 200 K would have identified 52% of all OTs. In other words, if one were to apply a simple 220 K IRW BT threshold to an image, all OT pixels would likely be identified. Unfortunately, quite a number of other non-convective cirrus cloud pixels would also be detected. Thus, one must take advantage of the characteristic that an OT is an “isolated region” of cold BT relative to the surrounding anvil cloud in order to reduce false OT detects. In order to find these cold BT regions, we compute spatial IRW BT gradients or “texture”, which is why the method is named “IRW-texture”.

The difference between the minimum OT and the mean surrounding anvil BT was calculated for these 450 storms to estimate how much colder an OT is than the surrounding cloud. For the grey curve in the Fig. 7, the mean anvil BT is computed by manually sampling the anvil temperature at an 8 km radius from the OT minimum BT location in 16 directions. An 8 km radius was selected in order to ensure that regions generally outside the OT are being sampled. For the 450 cases described above, the largest OT region subjectively identified in both IRW and visible channel imagery had a diameter of 12 km. Other studies by the authors have found some OTs with diameters of greater than 15 km. Figure 7 shows that $\sim 90\%$ of cases had minimum OT-mean anvil BT difference value greater than 6 K. The 50th percentile of this difference is near 9.5 K.

In summary, most OTs are less than 15 km in diameter with a maximum IRW BT of 220 K and a minimum OT-mean anvil BT difference of 6 K. A test of the 220 and 6 K parameters on an additional set of non-enhanced-V OT cases showed that too many false detections were produced. We have since adapted these criteria to require a minimum BT of 215 K and OT-mean anvil BT difference of 6.5 K to reduce false alarm at the expense of some detection capability.

The ABI OT detection algorithm based upon these concepts is shown in flowchart form in Figure 1, in graphical form in Figure 8, and will be summarized in the following text. The algorithm input data requirements are: 1) ABI Channel 14 11.2 μm IRW BT imagery and 2) NWP model tropopause temperature data. After variable initialization and reading of input datasets, cloudy pixels with IR window BT less than or equal to both 215 K and the NWP tropopause temperature are found. We include the NWP tropopause temperature information to ensure that a given pixel is indeed “overshooting” the tropopause. The tropopause height from the NWP model is based upon the level of the coldest temperature in the vertical profile. The GFS has been the NWP model most often used in algorithm testing up to this point in time, but this algorithm can operate

effectively with any NWP tropopause temperature data, provided the data is interpolated to the ABI navigation within the FRAMEWORK.

The next step involves sorting the list of cold pixels by their IR window temperature into a 1-D array, with the coldest pixel being first. We call these pixels “candidate OT pixels”. The distance between the candidates and their neighboring pixels is then computed to find the pixel spatial resolution at the candidate OT location. This local spatial resolution is used to determine the number of ABI pixels required to cover an 8 km distance. The algorithm then loops through this 1-D array to evaluate the mean surrounding anvil BT for each pixel. The algorithm samples the anvil at an 8 km radius in 16 directions to compute this mean. A pixel with an IRW temperature of 225 K or colder must be present for at least 5 of the 16 radii for a valid mean to be computed. A $\text{BT} \leq 225 \text{ K}$ is considered to be representative of an optically thick cirrus anvil cloud. The 5 of 16 pixel criteria is imposed to ensure that the anvil is of relatively large horizontal extent, but allows for situations when an anvil is confined to a 90 degree quadrant as can be the case when strong upper-level winds direct the storm outflow in a narrow region. The candidate OT pixel is placed into a final OT array if the candidate is at least 6.5 K colder than the mean surrounding anvil BT.

At this point, only the coldest pixel of each OT has been identified, which we call the “OT center”. The last step involves filling in the entire overshooting region, as OTs can be greater than 15 km in diameter. Pixels within a 15 km region that are at least 50% colder than the mean surrounding anvil BT are classified as OT pixels. For example, if the IRW BT of an OT center is 190 K and the surrounding anvil mean BT is 210 K, then all pixels within the search region with $\text{BT} \leq 200$ are also considered OT pixels. This threshold would be 195 K if the anvil mean BT were 200 K. After all remaining OT pixels are identified, an output file is written and the algorithm terminates.

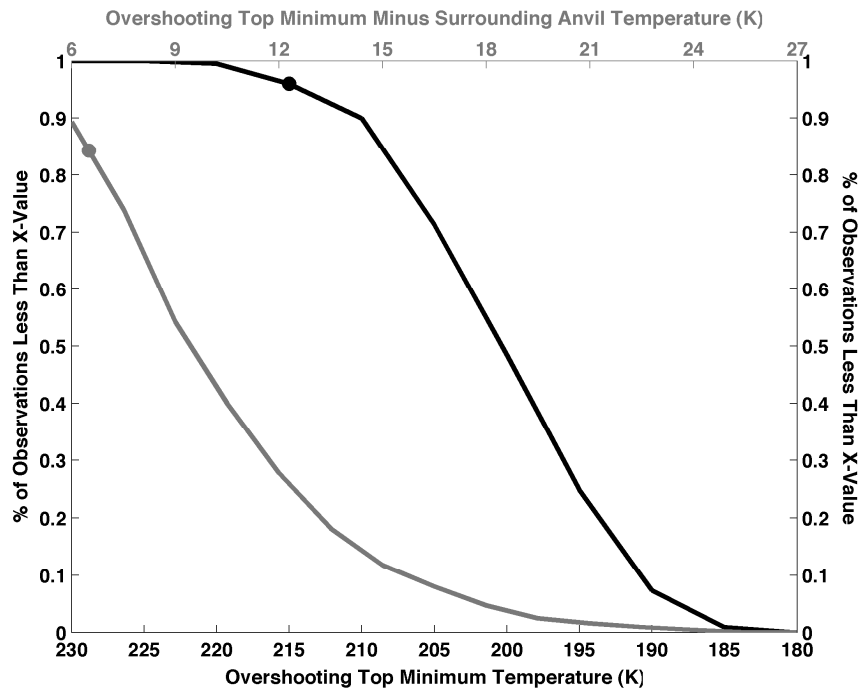


Figure 7 - (black line) The frequency of OT minimum IRW BTs less than BT values along the bottom x-axis scale for 450 enhanced-V producing thunderstorms described by Brunner et al. (2007). (grey line) The frequency of the OT minimum BT minus mean surrounding anvil BT less than BT difference values along the top x-axis scale for the same 450 thunderstorm database. Circles along the two lines represent criteria used in the IRW-texture OT detection method.

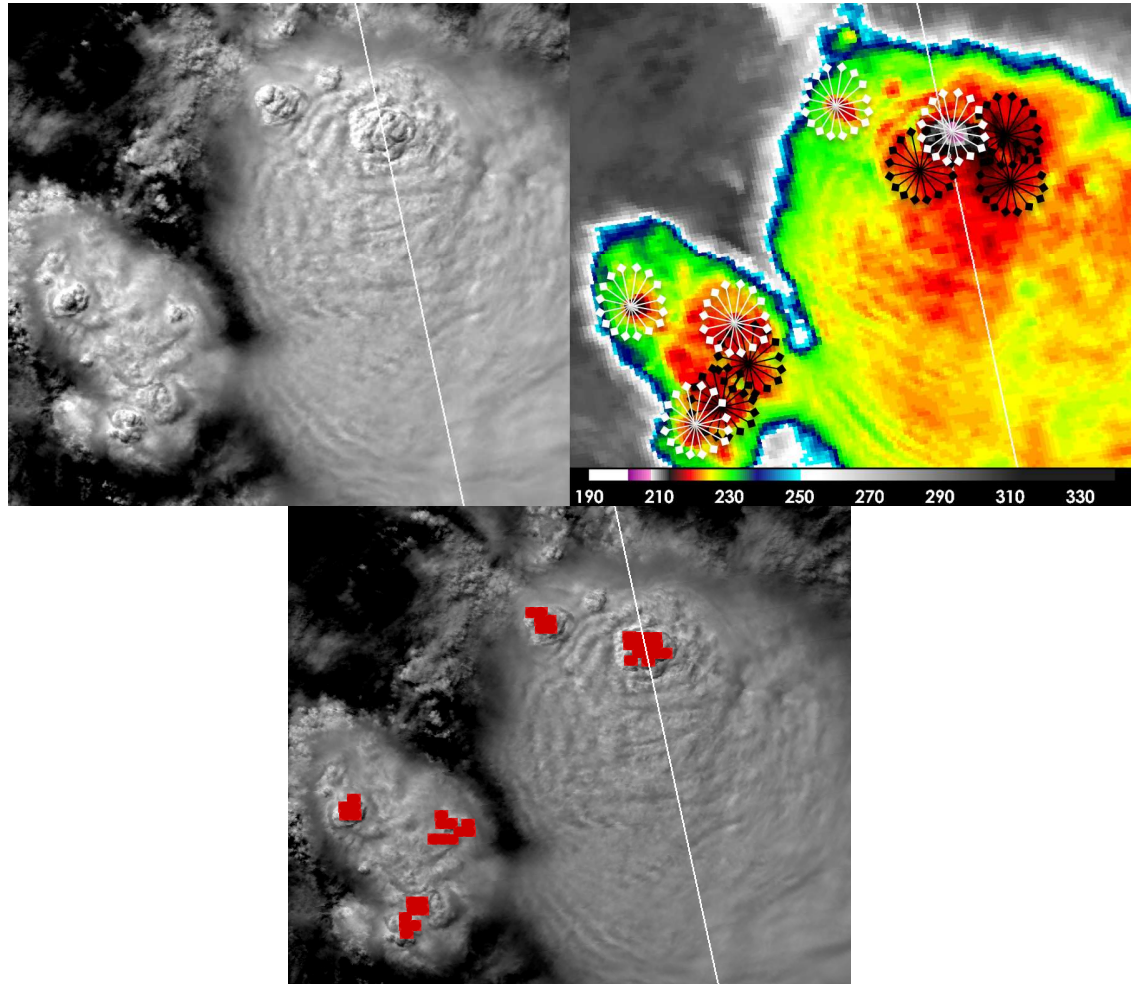


Figure 8 - A graphical example of the ABI overshooting top detection algorithm. (top-left) MODIS 250 m visible channel image at 2315 UTC on 5/9/2008. (top-right) MODIS 1 km IRW image at the same date and time. The center of a cluster of black lines indicates a pixel with an IRW BT less than or equal to 215 K and the NWP tropopause temperature that is not at least 6.5 K colder than the surrounding anvil. The end point of each of the black lines shows the 16 pixels that were included in the mean anvil BT calculation. The center of a cluster of white lines indicates a cold pixel that is also significantly colder than the surrounding anvil and is therefore considered an overshooting top pixel. (bottom) The final OT detection field (red pixels) after the remaining pixels that compose the OT are identified. The diagonal white line extending across the three images shows the location of a CloudSat overpass that will be discussed later.

3.4.1.2 Objective Enhanced-V Signature Detection

An enhanced-V signature is composed of the following in IRW satellite imagery (see Figure 9 for an example):

- 1) An OT which is well correlated with the coldest pixels in a given thunderstorm cloud top and acts to divert the upper level flow around it.
- 2) A U- or V-shaped pattern of relatively cold BTs with the apex of the U or V signature located slightly upwind of the OT. The “arms” of this signature extend downwind of the OT, often along the periphery of cirrus anvil cloud.
- 3) A region of anomalously warm BTs located downwind of the OT region. The combination of the cold OT and downstream warm region is called the anvil thermal couplet (ATC).

McCann (1983) and Brunner et al. (2007) describe the relationship of storms exhibiting the enhanced-V signature to severe weather such as strong winds, large hail, and tornadoes. Brunner et al. shows that an ATC with a large OT-warm region BT difference is a strong indication that the parent thunderstorm is severe. The AVHRR image in Fig. 9 shows a pronounced cold V-shaped signature with a significant warm area enclosed by the “arms” of the V. Negri (1982) and Heymsfield et al. (1983) hypothesize that the downstream warm area is produced through adiabatic descent (or subsidence) downwind of the OT updraft location. Others such as Setvak et al. (2007) suggest that moisture ejected into the stratosphere produces an “above anvil cirrus plume” downstream of the OT, which radiates at a warmer temperature than the primary anvil cloud underneath.

Figure 10 and Brunner et al. (2007) show that the enhanced-V signature appears differently in almost every case, making direct pattern recognition of this feature nearly impossible. In addition, as spatial resolution decreases, the V pattern becomes poorly defined in IRW imagery (see Figure 11). Despite the coarser GOES-12 spatial resolution, the downstream warm area component of the ATC is still apparent. We therefore focus our effort on objective ATC detection rather than direct pattern recognition of the enhanced-V signature. The algorithm will be called the “enhanced-V ATC detection algorithm” for the remainder of this document.

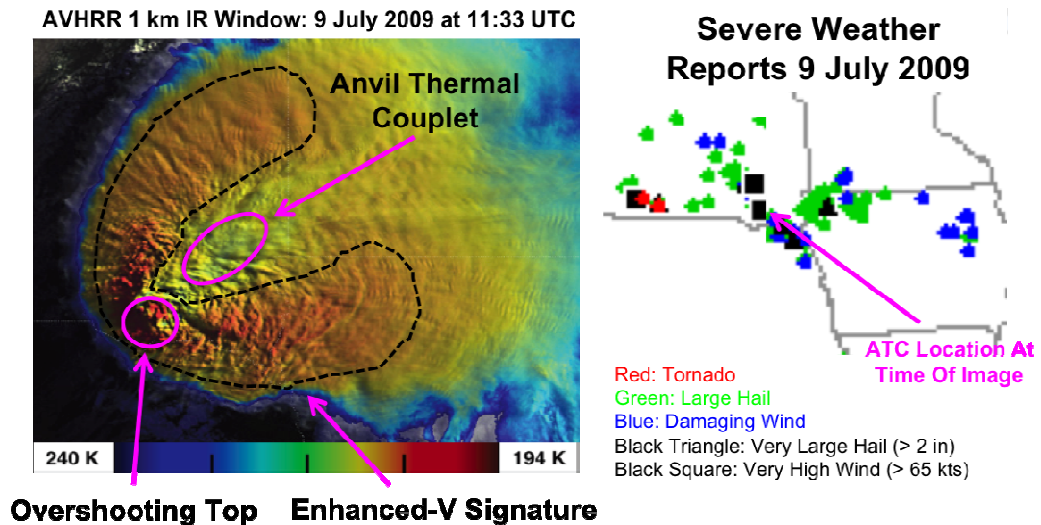


Figure 9 - (left) An example of an enhanced-V signature present in 1 km AVHRR 10.8 μm IRW imagery on 9 July 2009 at 1133 UTC. The IRW imagery is superimposed atop visible channel imagery, giving the image a pseudo 3-D appearance. (right) Severe weather reports on 9 July 2009. The location of the storm shown in the left panel is indicated.

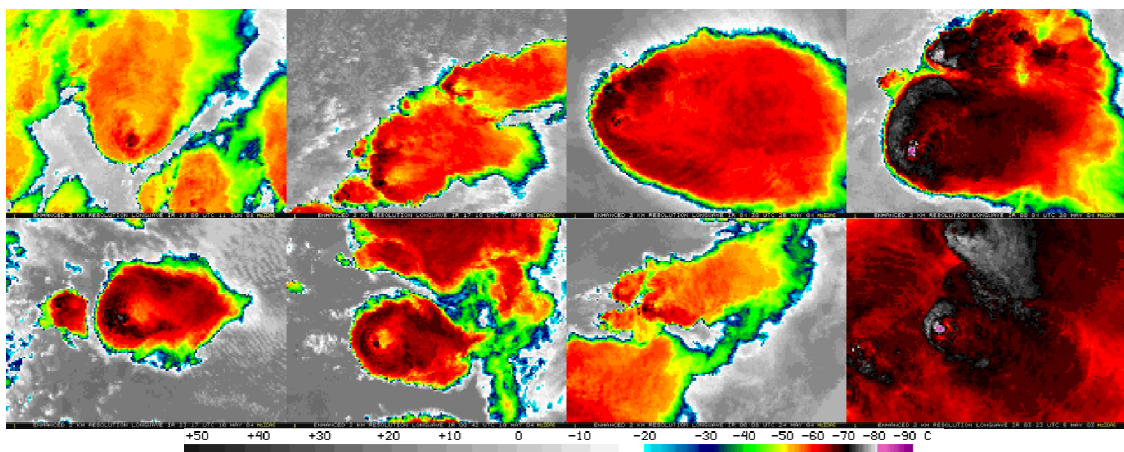


Figure 10 - MODIS and AVHRR ~11 μm IR window imagery for 8 enhanced-V events. All images cover the same horizontal distance and use same color enhancement, illustrating the significant variations in the V-signature across events.

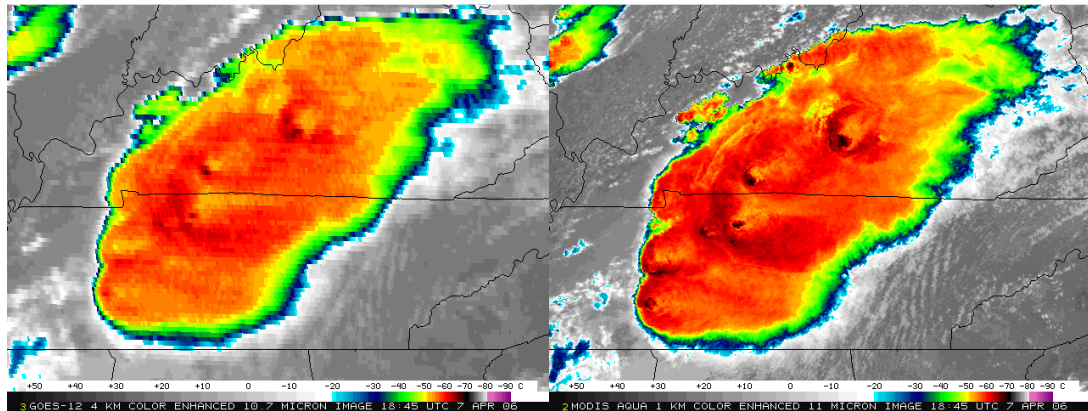


Figure 11 – (left) GOES-12 and (right) MODIS 10.7 μm IRW imagery for a thunderstorm complex with several enhanced-V signatures.

3.4.1.2.1 The ABI Enhanced-V ATC Detection Algorithm

The following discussion will focus on the components of and logic behind the ABI enhanced-V ATC detection algorithm. Figure 2 provides a flowchart and Figure 12 provides a schematic representation of the ABI enhanced-V ATC detection algorithm that will be described in detail here. The algorithm begins by reading in the locations of OT “centers” detected by the ABI OT algorithm. The next step involves a search to identify a downstream warm region that is “coupled” with this OT over a box that contains all pixels 25 km to the east, north, and south of an OT to identify a downstream warm region that is “coupled” with this OT. As ATC detection is only required for ABI CONUS and Mesoscale domains, the search for an ATC is limited to the eastern 180° sector. Brunner et al. (2007) show that enhanced-V features and their associated ATC are oriented to the eastern side of the OT due to prevailing upper-level winds that nearly always have some westerly wind component over CONUS. Figure 13 shows that, of the 450 enhanced-V cases in the Brunner et al. database, the downstream warm region was within 25 km of the OT for 97% of events. Thus, 3% of ATC cases could be missed through limiting the size of the search box to a 25 km distance from the OT. However, warm regions in the northeast or southeast direction from the OT could be detected up to a 35 km distance from the OT (via the Pythagorean Theorem) through the use a 25 km search box.

Within the search box, the 3x3 pixel mean IRW BT is used to identify candidate downstream warm areas. A 3x3 pixel region is used to eliminate false detections from single pixels with abnormally warm BTs due to sensor noise. In addition, a minimum distance threshold check is performed between the center pixel of the 3x3 pixel candidate warm region and the OT location. The candidate warm region must be at least 6 km from the OT location for it to be further considered as a warm region.

Figure 14 shows that the downstream warm region maximum BT was colder than 225.0 K for 95% of these cases. Figure 15 indicates that the difference between the OT and downstream warm area maximum BT is greater than 12 K for 70% of the cases. In summary, through a combination of these findings and experimentation on a variety of satellite scenes with ATCs being present, the downstream 3x3 warm region mean BT in the ABI ATC algorithm must be 1) at or colder than 225.0 K, 2) between 6 and 35 km

away from an OT, and 3) at least 12 K warmer than the OT. The 12 K difference threshold has the biggest impact on enhanced-V ATC detection capability, limiting the POD to 70% based on the Brunner et al. 450 case database. However, the 12 K difference threshold is chosen because it eliminates more false detections compared to smaller magnitude difference thresholds.

The candidate warm region 3x3 pixel maximum BT is then compared to the surrounding pixels within a 25 km box centered on the candidate warm region. All of the pixels within this 25 km box must be at or colder than the candidate 3x3 warm region maximum BT. This test is done to ensure that the candidate warm region is positioned within the anvil cloud and is not along the edge of the anvil, since warm regions associated with enhanced-Vs are not located along the anvil edge. Next, the candidate warm region 3x3 pixel mean BT is compared to the surrounding anvil to ensure that the couplet represents a focused area of relatively warm BT usually found with an enhanced-V ATC. The surrounding anvil is sampled at a 15 km radius at equally spaced 45-degree angles. 7 of the 8 sampled pixels must be at or colder than the candidate 3x3 warm region mean BT.

A final test is performed to ensure that the candidate warm region is surrounded by a relatively large expanse of colder anvil cloud pixels. This test also has the effect of eliminating situations where an ATC is misclassified due to the presence of an anvil cloud edge or close proximity to another nearby weaker thunderstorm with warmer tops. The image line and element locations are computed for a ray that extends from the OT center directly through the candidate warm region and out to a 50 km distance beyond the candidate warm region. The mean BT is calculated for 3x3 pixel regions centered on each line/element of this ray. The mean BTs along this ray cannot be warmer than the maximum BT of the candidate warm region, which ensures the presence of a continuous anvil cloud with a singular warm area. In addition, the 3x3 pixel mean BT of the ray end point must be at least 1 K colder than the maximum temperature of candidate 3x3 warm region to further ensure that the candidate warm area is indeed surrounded by colder pixels.

Once all of the candidate warm regions are identified for an associated OT, the candidate warm region with the largest BT difference between the OT center temperature and the candidate 3x3 pixel warm region mean BT is chosen. If the chosen candidate warm region is not within 15 km of another chosen warm region for a previous OT, then it is considered the ATC for the associated OT. However, if it is within 15 km of another ATC for a previous OT, then the OT/warm region couplet with the largest magnitude is chosen and the other OT/warm region couplet is discarded. The processing described above is repeated for each OT center pixel and the algorithm terminates after the final OT.

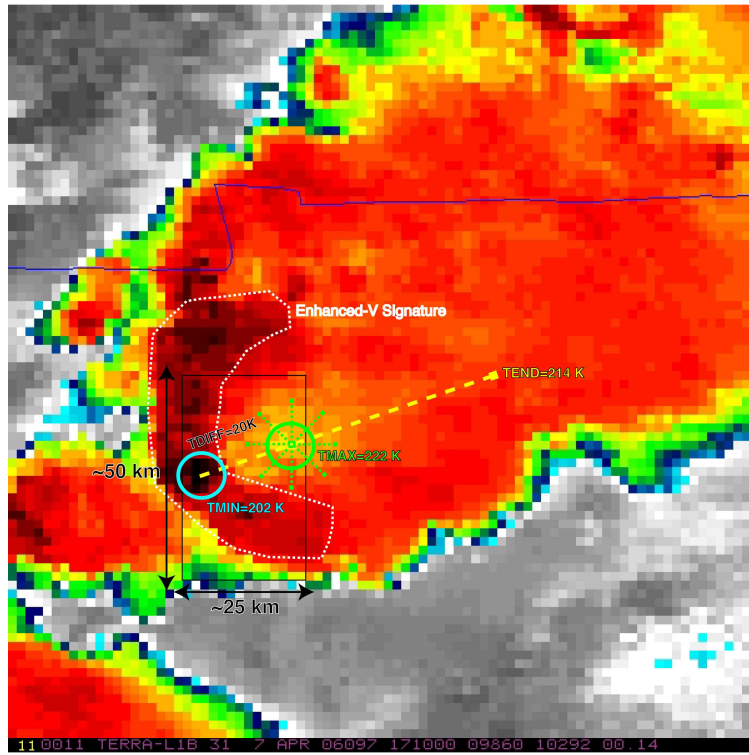


Figure 12 - A schematic representation of the ABI ATC detection algorithm using MODIS IR window imagery degraded to the 2 km ABI IR resolution for an enhanced-V case in Tennessee. Labeled upon the graphic are the enhanced-V location (white dashed line), the downstream warm area search box (black), the OT minimum BT location (cyan), the downstream warm area location and maximum BT (green), and the ray extending 50 km beyond the warm area with end of ray BT (yellow)

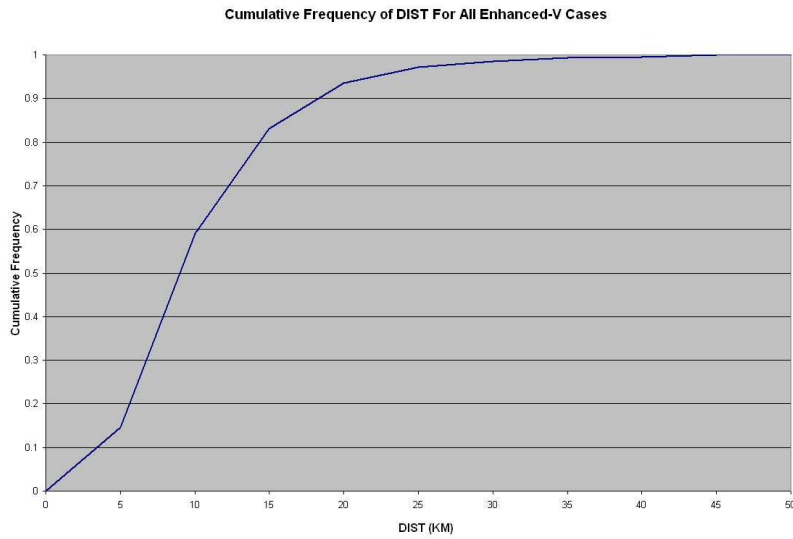


Figure 13 - A cumulative frequency diagram of the distance between the manually identified minimum IR window channel OT and downstream warm area BT for the 450 enhanced-V cases described by Brunner et al. (2007).

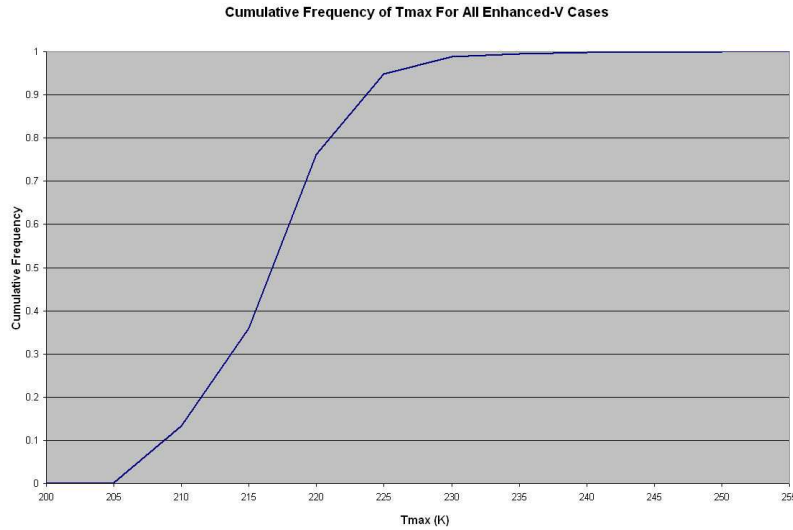


Figure 14- A cumulative frequency diagram of the manually identified downstream warm area maximum IR window channel BT for the 450 enhanced-V cases described by Brunner et al. (2007).

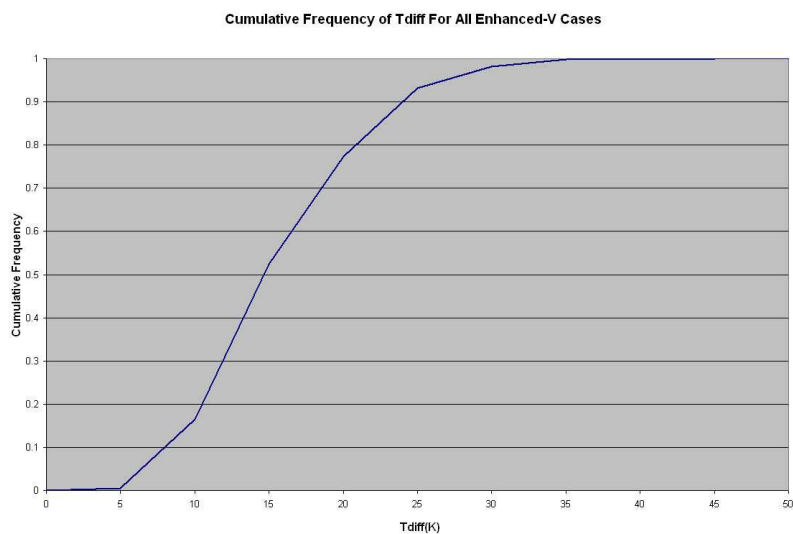


Figure 15 - A cumulative frequency diagram of the difference between the OT minimum and downstream warm area maximum BT for the 450 enhanced-V cases described by Brunner et al. (2007).

3.5 Algorithm Output

The final output of the overshooting top (OT) mask is a binary yes/no value indicating the presence of an overshooting pixel.. The OT algorithm output values and description are given below in Table 3.

The final output of the anvil thermal couplet (ATC) mask indicates the presence of a significant overshooting top/downstream warm area temperature difference. The ATC algorithm output values and description are given below in Table 4.

A set of quality assurance flags and metadata for both the OT and ATC algorithms are described in Tables 5-8.

In addition, these algorithms derive the following products that are not included as requirements in the F&PS, but serve as useful quality control information. These parameters along with their corresponding AIT FRAMEWORK NetCDF output variable names are provided in Table 9.

Overshooting Top Mask Value	Description	AIT FRAMEWORK Variable Name
Yes (1)	Pixels that meet all OT detection algorithm criteria	Overshoot_Grid_Flag
No (9999)	Pixels that failed an OT detection algorithm test	

Table 3 – A description of the overshooting top detection output from the ABI OT algorithm.

Anvil Thermal Couplelet Mask Value	Description	AIT FRAMEWORK Variable Name
Yes (1)	Overshooting pixels that have an anvil thermal couplet	Overshoot_Couplelet_Grid_Matching_ID
Yes (2)	Location of center of downstream warm region	
No (9999)	Pixels that failed an enhanced-V anvil thermal couplet detection algorithm test	

Table 4 - A description of the anvil thermal couplet output from the ABI ATC algorithm.

Quality Assurance Flag Value	Explanation
0	Pixel is an overshooting center
1	Pixel is classified as overshooting via fill procedure. Pixel is 50% colder than the mean surrounding anvil BT
2	Pixel is not classified as OT because its IRW BT is warmer than 215 K
3	Pixel is not classified as OT because its IRW BT is warmer than NWP tropopause temp
4	Candidate pixel is not classified as OT because it is located less than 15 km from another colder overshooting candidate pixel
5	Candidate pixel is not classified as OT because of an insufficient number (less than 5) of valid anvil pixels present at 8 km radius from overshooting candidate
6	Candidate pixel is not classified as OT because of an insufficient IRW BT difference (less than 6.5 K) between overshooting candidate and mean surrounding anvil BT
7	Candidate pixel is not classified as OT because it is located at greater than 70° local zenith angle

Table 5 – A description of the quality assurance flag values for the ABI OT algorithm

Metadata Description
Number of detected overshooting centers (i.e. “tops”)
Number of detected overshooting pixels
Number of pixels with IRW BT < 215 K but not colder than NWP tropopause temp
Mean IRW BT of overshooting pixels
Number of pixels that meet each of the 8 QA flag criteria
Definition of QA flag criteria

Table 6 – A description of the metadata for the ABI OT algorithm

Quality Assurance Flag Value	Explanation
0	Pixel is an overshooting top with a thermal couplet
1	Pixel is at the center of the downstream warm region
2	Candidate warm region pixel is selected because it is either less than 6 km from overshooting center or outside a 25 km (to the east of OT center) x 50 km (25 km to the north/south of OT center) search region
3	Candidate warm region pixel is not selected because at least one pixel within 3x3 box surrounding it is warmer than 225 K
4	Candidate warm region pixel is not selected because the magnitude of difference between overshooting center IRW BT and 3x3 mean BT for box surrounding it is less than 12 K
5	Candidate warm region pixel is not selected because the 3x3 maximum BT for box surrounding it is colder than at least one pixel within a 25 km region
6	Candidate warm region pixel is not selected because less than 7 pixels at a 15 km radius from it have an IRW BT at or colder than warm region 3x3 mean BT
7	Candidate warm region pixel is not selected because the couplet ray test has failed
8	Candidate warm region pixel is not selected because a different candidate warm region pixel associated with the same overshooting center has a larger overshooting center IRW BT – warm region 3x3 mean BT difference
9	Tests 2 through 8 passed, but candidate warm region pixel is not selected because it is within 15 km of another warm region for a different overshooting center

Table 7 - A description of the quality assurance flag values for the ABI ATC algorithm

Metadata Description
Number of detected overshooting centers (i.e. “tops”)
Number of overshooting centers with an anvil thermal couplet
Number of pixels that meet each of the 10 QA flag criteria
Definition of QA flag criteria

Table 8 - A description of the metadata for the ABI ATC algorithm

Quality Control Field Description	AIT FRAMEWORK Variable Name
OT identification number	Overshoot_Grid_ID_Num
Number of pixels used in computation of mean BT for the anvil cloud surrounding the OT	Overshoot_Grid_Num_Anvil_Pix
Minimum Channel 14 IRW BT within the OT	Overshoot_Grid_BT
BT difference between the OT minimum BT and mean surrounding anvil BT	Overshoot_Grid_Magnitude
ATC ID number recorded at the ATC mask location which matches that of its parent OT ID number	Overshoot_Couplet_Grid_Matching_ID
BT difference between the OT minimum BT and the ATC BT	Overshoot_Couplet_Grid_BT_Diff

Table 9 – A description of additional quality control parameters included in OT and ATC algorithm AIT FRAMEWORK output.

4 TEST DATA SETS AND OUTPUTS

4.1 Simulated/Proxy Input Data Sets

Advanced Very High Resolution Radiometer (AVHRR) and Aqua/Terra MODIS IRW BTs are used as the primary proxy ABI satellite inputs to the IRW-texture OT and the enhanced-V ATC detection algorithms. These 1 km satellite data are degraded and remapped to the 2 km ABI resolution and geostationary viewing projection. AVHRR data is acquired from the NOAA Comprehensive Large Array-data Stewardship System (CLASS). MODIS data is acquired from the NASA Level 1 Atmosphere Archive and Distribution System (LAADS). The algorithm has also been tested successfully with 3 km resolution MSG SEVIRI data.

Version 2.2 of the ARW (Advanced Research core of the Weather Research and Forecasting (WRF)) model (Skamarock et al. 2007) was used to generate a high-resolution simulation of a widespread convective storm event that occurred over the central U.S on 4-5 June 2005. Synthetic ABI IRW channel BTs are generated from ARW output and are used as input to the ABI OT detection method (Otkin et al. 2009). These simulated BTs are at a 2 km spatial resolution and 5 min temporal resolution and were produced every 5 mins over CONUS. The time period of the ARW simulation between 2200 and 0000 UTC was used by Bedka et al. (2010) to examine the accuracy of the ABI OT detection method. See http://cimss.ssec.wisc.edu/goes_r/awg/proxy/nwp/ncsa_fcm/index.html for a full WRF model simulation description of the above simulation.

4.2 Validation Truth Data Sets and Methodology

4.2.1 CloudSat OT Observations

The CloudSat Cloud Profiling Radar reflectivity factor product (2B-GEOPROF, Stephens et al. 2002; Mace et al, 2007) is used to identify OT events observed by CloudSat during the April '08 to September '09 time period. The footprint of a CloudSat CPR profile covers 1.7 km in the along-track direction and 1.3 km in the across-track direction. A new profile is captured every 1.1 km, indicating that there is some overlap between adjacent profiles (i.e. oversampling). The effective vertical resolution is 480 m, with oversampling at a 240 m resolution. The 2B-GEOPROF product provides a cloud mask and radar reflectivity at each of the 125 vertical data bins. A cloud mask value ≥ 20 is used to identify clouds and locate cloud tops. See the “CloudSat Data Users Handbook” for additional detail on CloudSat and the 2B-GEOPROF product.

Possible CloudSat observations of OTs were identified through subjective analysis of archived 2B-GEOPROF quicklook imagery available on the Colorado State University CloudSat Data Processing Center (DPC) webpage (<http://www.cloudsat.cira.colostate.edu/>). Imagery from nearly 3000 CloudSat data granules were investigated over the 1.5 year period mentioned above. After the list of possible OT events is developed, the 2B-GEOPROF product for these events is acquired from the CloudSat DPC and each possible event is carefully analyzed to verify the presence of a protrusion above an NWP tropopause height analysis and the surrounding anvil cloud top, which is consistent with the conceptual model of an OT (Adler and Mack 1986; Wang 2003). The highest cloud top must be at least 0.5 km above the surrounding anvil cloud for two adjacent CloudSat profiles to ensure the presence of a coherent OT signature. This implies that the smallest OT in the final OT database can be ~ 2.8 km in diameter in the along track direction. For daytime events, Aqua MODIS 250 meter spatial resolution visible imagery along the CloudSat overpass is also analyzed to further verify that CloudSat observed an OT. OT events that meet these criteria are assigned to the final OT database. A total of 114 OT events were found during the April '08 to September '09 study period. While it may be possible to develop an automated objective CloudSat OT identification method that could identify a greater number of OT events, based on our experience in CloudSat 2B-GEOPROF data analysis, we feel that manual investigation combined with MODIS visible image analysis (when available) offers the most definitive and accurate means for determining OT events.

CloudSat-observed OTs are treated as both single coherent entities (i.e. “top regions”) and as the individual pixels that compose the top. This distinction is important because a detection method may not identify every pixel within an OT along the CloudSat track but could identify some portion of the top region. If some portion of the top region is detected, this should be rewarded within the validation framework as the detection algorithm has identified a potentially hazardous thunderstorm with a strong updraft. The exact location and spatial extent of an OT is subjectively determined through examination of the CloudSat 2B-GEOPROF profile. In addition to the pixels within the relatively small OT regions, a large sample size of non-overshooting deep

convective cloud pixels along the CloudSat overpass are also included for each of the 114 events, providing ample opportunity for errant detection.

The following metrics are used to evaluate the accuracy of ABI OT detections: 1) OT pixel FAR and 2) probability of detection (POD) of all possible top regions. An OT pixel POD cannot be accurately determined here because either detection method would be penalized if the storms moved in the 2-min time interval between MODIS/CloudSat observations and the OT detections did not match all CloudSat-observed OT fields of view.

OT pixel detections (metric 1) are considered accurate if they are found within a region extending 5 km outside the bounds of the subjectively-determined CloudSat OT location. The distance window outside the OT is used here to account for storm movement/evolution in this 2-min time interval and other possible navigation and/or co-location induced errors. The OT pixel FAR is defined as:

$$\text{OT Pixel FAR} = \frac{\text{Number of incorrect OT pixel detections}}{\text{Total number of OT pixel detections}}$$

A top region is accurately detected if at least one synthetic ABI detection pixel is found within the bounds of the CloudSat observed OT region (metric 2). The probability of detection (POD) for all possible top regions is defined as:

$$\text{Top Region POD} = \frac{\text{Total number of accurately detected top regions}}{\text{Total number of CloudSat observed top regions}}$$

4.2.2 WRF ARW Simulated OT Events

ARW model output is used here to identify “truth” OT pixels and validate synthetic ABI-based detections. Once truth OT pixels are identified, the validation is trivial since ARW output is used to generate the synthetic ABI BTs and the map projection and horizontal resolution of the two datasets are an exact match. The total hydrometeor mixing ratio (THMR), which represents a summation of the rain, graupel, snow, pristine crystal, and cloud liquid water content at each ARW model vertical level, is used to define the truth OT locations. Animated ARW cloud isosurfaces and vertical motion fields show that anomalously large THMR values in the lower stratosphere are indicative of strong thunderstorm updrafts and OTs. An example of the relationship between two ARW-simulated OTs and the THMR at 200, 175, and 150 hPa is shown in Figure 16.

The ARW cloud top height is defined as the highest model level where a THMR $\geq 0.05 \text{ g kg}^{-1}$ is present. During this time period, the tropopause was found to be at $\sim 175 \text{ hPa}$ ($\sim 13 \text{ km}$) over the convectively active portion of the domain. As the ARW simulation at these levels has a 0.5 km vertical resolution, ABI OT detections are

compared with two sets of pixels, those with cloud tops above 175 hPa and 165 hPa (~13.5 km). As the ABI OT detection method may detect overshooting of varying magnitude, two truth OT criteria are used to identify both marginal (cloud height: 175 to 165 hPa, 0-0.5 km overshooting magnitude) and more significant (< 165 hPa, > 0.5 km) OT occurrences.

A second indicator of algorithm performance involves comparison of synthetic ABI OT detections to a smaller set of “high confidence” OT pixels. These pixels are defined using two criteria: 1) cloud top heights \leq 125 hPa (~15 km, 2 km overshooting magnitude) and 2) an anomalously high THMR at the tropopause. Based upon these criteria, the pixels would be associated with intense vertical motions in the upper troposphere and lower stratosphere and would correlate well with significant overshooting. In order to determine anomalously high tropopause THMR, 175 hPa ARW THMR values are accumulated across the entire CONUS domain over the two hour ARW study period and a distribution of this data is produced. Pixels with a THMR exceeding the 99th percentile at 175 hPa and height \leq 125 hPa are considered high confidence OT pixels.

OT pixels detected in synthetic ABI imagery are compared to these two sets of “truth” pixels to derive quantitative performance statistics. Two statistics will be used to evaluate the relative accuracy of the IRW-texture technique, 1) false alarm rate and 2) probability of high confidence OT pixel detection. The false alarm ratio (FAR) is defined as:

$$FAR = \frac{\text{Number of Incorrect OT Pixel Detections}}{\text{Total Number of OT Pixel Detections}}$$

The probability of high confidence OT pixel detection (POD) is defined as:

$$POD = \frac{\text{Total Number of Correctly Identified High Confidence OT Pixels}}{\text{Total Number of High Confidence OT Pixels}}$$

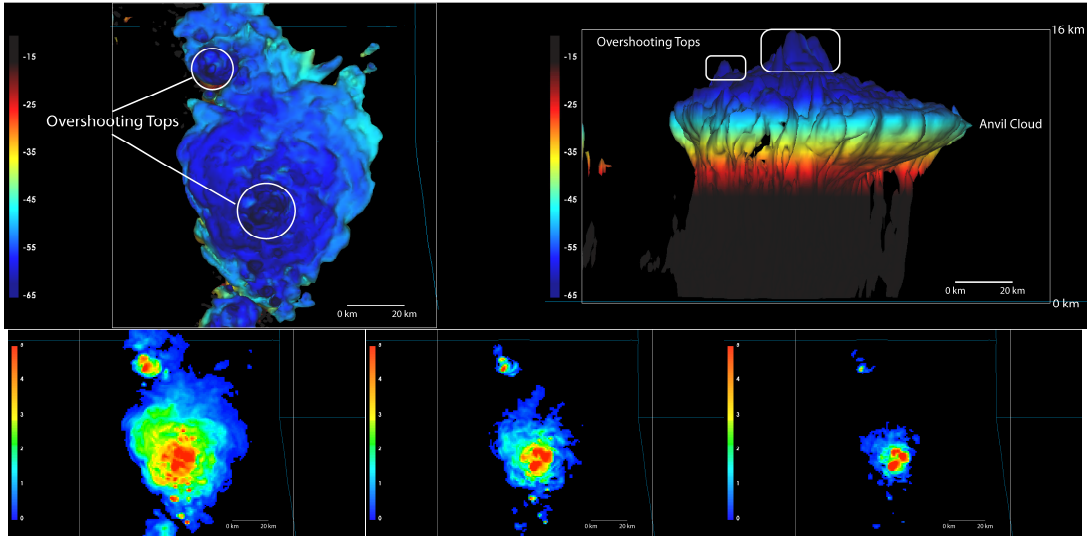


Figure 16 - (upper-left) A top view of the 0.05 g/kg THMR isosurface colored by simulated GOES-R ABI 11.2 μm IRW BTs. OTs appear as localized cold regions surrounded by a warmer anvil cloud. Warm temperatures for clear sky and low cloud pixels are transparent. (upper-right) A side view of the same isosurface showing that the two OTs have heights significantly higher than the anvil cloud. The isosurface is colored here by the ARW 3-D temperature field. ARW THMR output at 200 hPa (lower-left), 175 hPa (lower-middle), and 150 hPa (lower-right) showing that high THMR values are associated with the OTs identified in the top panels. Graphics were produced using the McIDAS-V visualization software developed at UW-SSEC.

4.2.3 MODIS + AVHRR Enhanced-V and ATC Database

The ATC detection algorithm has been tested on 55 MODIS and AVHRR images where enhanced-V signatures have been subjectively identified. Many of these images have more than one enhanced-V signature in the image. These 55 cases contain a total of 203 enhanced-V producing storms, in addition to ~ 2000 storms that do not have an enhanced-V signature. The relatively large sample size of both V-signature and null events provides ample opportunity for the ATC algorithm to succeed and fail. These 203 events are a subset of the 450 events identified and described by Brunner et al. (2007).

Proxy ABI imagery for these 55 cases are processed within the ATC detection algorithm. Output is compared with known locations of enhanced-V signatures in the proxy ABI imagery. POD and FAR are the statistics used here to evaluate the skill of the ABI ATC detection algorithm. FAR is defined as:

$$FAR = \frac{\text{Number of Incorrect Enhanced-V ATC Detections}}{\text{Total Number of Enhanced-V ATC Detections}}$$

POD is defined as:

$$POD = \frac{\text{Total Number of Correctly Identified Enhanced-V ATCs}}{\text{Total Number of Enhanced-V ATCs}}$$

4.3 Output from Simulated/Proxy Input Data Sets

4.3.1 MODIS-Based Proxy ABI OT Detections and Comparison With CloudSat OT Observations

This section begins with a discussion of two CloudSat-observed OT events and the associated OT detection fields. Figure 17 shows a deep convective cloud over the South Pacific that features a classic example of an OT, where a sharp BT minima and a lumpy appearance in the visible channel image is co-located with a significant OT signature in the CloudSat 2B-GEOPROF profile. The MODIS imagery for the Sudan OT case in Figure 18 shows very similar patterns to that of Figure 17, though the minimum IRW BT is much colder due to a higher tropopause level. Figure 19 shows that the ABI algorithm detected these CloudSat observed OTs in addition to several other likely OTs that are also present in these images.

OTs were most often observed by CloudSat over the tropics during the April 2008 to September 2009 time period (Figure 20). Only 12 of the 114 total OTs (11%) were found in the mid-latitudes. The Aqua satellite has an equatorial crossing time of 1:30 AM/PM local standard time, which does not coincide with the time period where deep convection is most often present in the mid-latitudes. OTs were found more often in the Northern Hemisphere because the 1.5-year study period covers two Northern Hemisphere warm seasons, but only one for the Southern Hemisphere. Figure 20 also shows that the CloudSat-observed OTs were better detected over land than those over water. Heymsfield et al. (2010) shows that the maximum upward vertical motion in land-based convection is of greater magnitude and at a higher vertical level than convection over ocean. Thus, OTs over land would likely be of larger magnitude and would therefore appear more prominently in IRW imagery, leading to a higher detection rate using the ABI IRW-texture method.

Validation statistics for the ABI OT detection method are shown in Table 9. Various WV-IRW BTD thresholds are evaluated here to determine if BTD magnitude can be used to increase detection performance to a level comparable with that of IRW-texture. The results show that both the pixel FAR and top region POD steadily decrease with increasing BTD. A positive WV-IRW BTD value can be used to identify nearly all top regions, but it is apparent that the vast majority of pixels that meet this BTD threshold are false detections. A BTD of $\geq \sim 1$ K is required to match the $\sim 74\%$ IRW-texture top region POD, but the pixel FAR for this BTD criterion (75%) would far exceed the $\sim 16\%$ IRW-texture FAR. A BTD of $> \sim 3$ K would be required to match the IRW-texture FAR, but the top region POD would be limited to 11.6% for this threshold. When NWP tropopause temperature information is included, the ABI IRW-texture method meets the OT algorithm accuracy requirement of 25% maximum FAR specified in the F&PS document.

Analysis indicates that 19 of the 29 (~66%) undetected OTs did not have cloud tops colder than the GDAS tropopause temperature, so these top regions were never

considered by IRW-texture (not shown). Based on this information, one might infer that the use of NWP tropopause information in the algorithm is adversely affecting OT detection performance. In order to test this, a version of the IRW-texture method that does not require an OT pixel to have an IRW temperature below that of the tropopause was applied to the 104 proxy ABI IRW BT datasets. Table 10 shows that the top region POD does increase when the GDAS tropopause temperature check is removed, but the FAR also increases significantly. Figure 21 shows the CloudSat CPR profile and MODIS imagery for an event where false OT detections were produced after removal of the tropopause temperature check. Figure 22 shows that the number of OT detections increases from 4 to 19 when this check is removed for this event. Analysis of MODIS imagery for these OT locations indicates that many of these additional detections correspond with IRW BT minima and enhanced visible channel texture, which are signatures typically associated with OTs. At the -6° latitude, the CloudSat CPR profile shows an overshooting magnitude of 0.25 km, which is less than the 0.5 km requirement used to identify cases for the CloudSat OT validation database. Based on this example, it is possible that some component of the additional FAR is caused by detection of marginal OTs that did not meet the criteria used to identify OT events in CloudSat data. The OT detections present along the CloudSat overpass at -7.4° latitude illustrates that removal of the tropopause temperature check also causes legitimate false OT detection. These results indicate that use of the NWP tropopause temperature information in the IRW texture method greatly minimizes false detection while preserving detection of a significant majority of OT events.

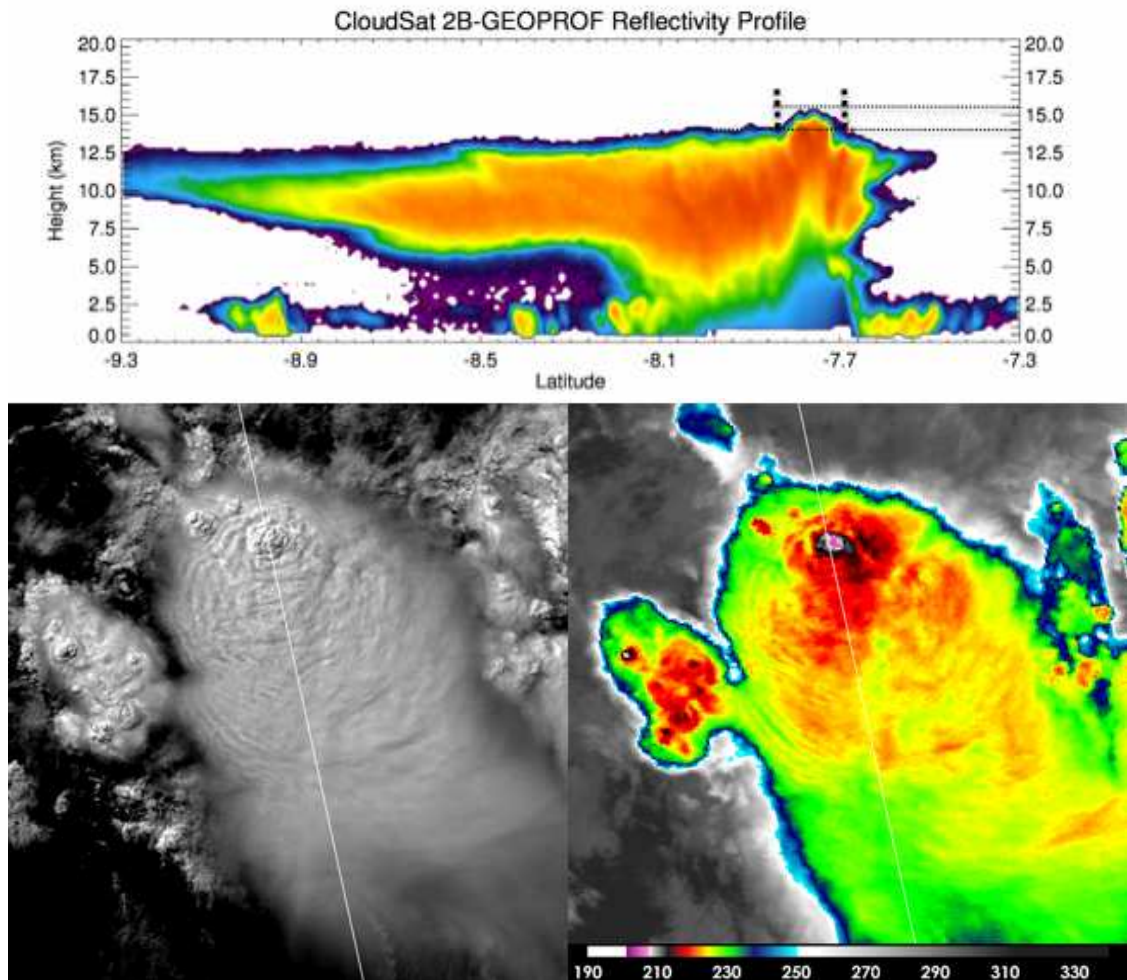


Figure 17 - (top) A CloudSat overpass of a deep convective cloud with an OT over the South Pacific on 9 May 2008 at 2317 UTC. The region within the two vertical dashed lines is the OT. The horizontal lines denote the peak height of the OT and the height of the anvil cloud surrounding the OT. (lower-left) Contrast-enhanced Aqua MODIS 0.25 km visible channel imagery at 2315 UTC. (lower-right) Color-enhanced Aqua MODIS 1 km IRW BT imagery. The white diagonal line in the bottom panels shows the location of the CloudSat overpass from the top panel.

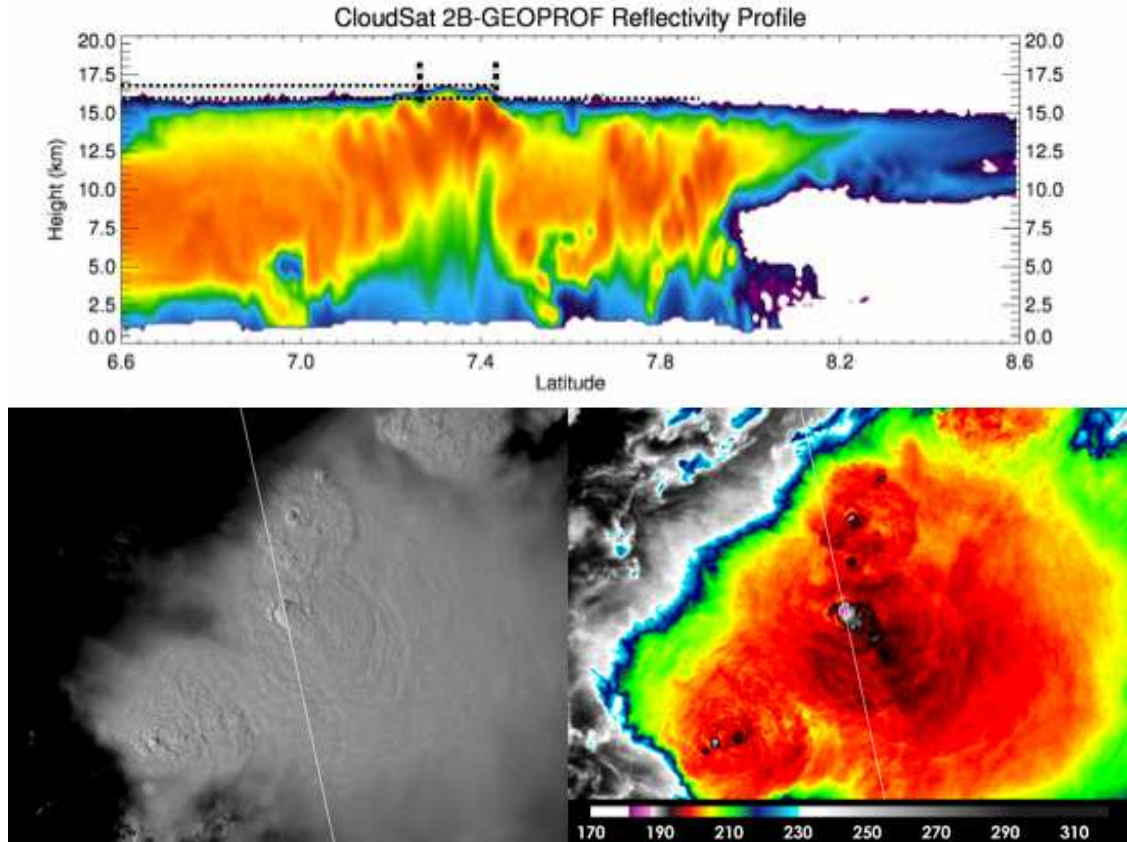


Figure 18 - (top) A CloudSat overpass of a deep convective cloud with an OT over the South Pacific on 9 October 2008 at 1142 UTC. The region within the two vertical dashed lines is the OT. The horizontal lines denote the peak height of the OT and the height of the anvil cloud surrounding the OT. (lower-left) Contrast-enhanced Aqua MODIS 0.25 km visible channel imagery at 1140 UTC. (lower-right) Color-enhanced Aqua MODIS 1 km IRW BT imagery. The white diagonal line in the bottom panels shows the location of the CloudSat overpass from the top panel. Note that the BT range of the color-enhancement of the lower-right panel differs from that of the corresponding panel in Figure 17.

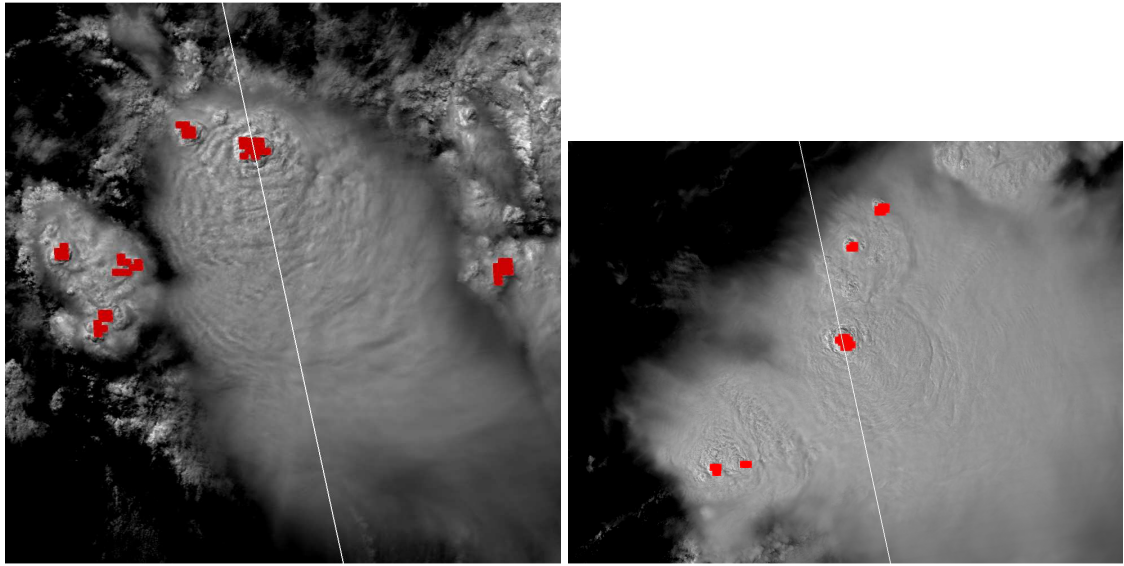


Figure 19 - ABI OT detections (red pixels) for the 9 May 2008 (left) and 9 October 2008 (right) cases shown in Figs. 17 and 18.

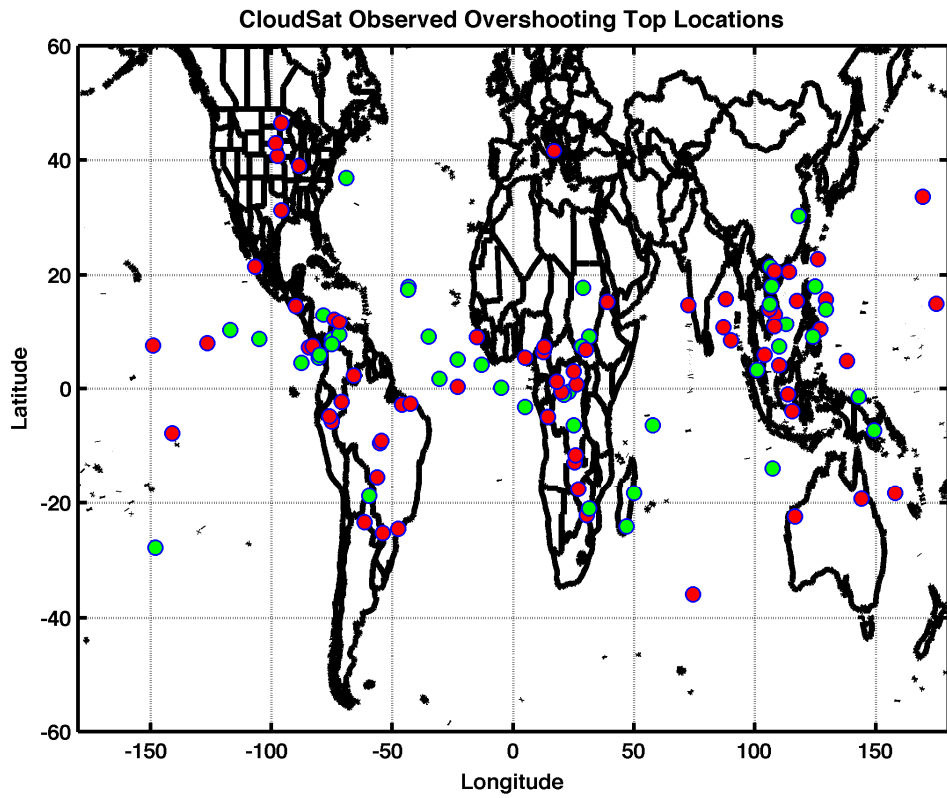


Figure 20 - A map of the 114 OTs identified within CloudSat CPR observations from April 2008 to September 2009. Red circles indicate OTs that were accurately detected by the ABI IRW-texture method and green circles indicate those that were undetected.

OT Detection Method	OT Pixel FAR	POD for Top Regions	Number of OT Detection Pixels Along CloudSat Track
IRW-texture (with GDAS Tropopause Temperature Check)	16.0%	75.4%	943
IRW-texture (without GDAS Tropopause Temperature Check)	60.0%	92.1%	2612
WV-IRW BTD ≥ 0 K	81.1%	96.4%	15469
WV-IRW BTD ≥ 1 K	75.0%	79.5%	7119
WV-IRW BTD ≥ 4 K	15.3%	11.6%	72

Table 10 – Validation statistics for the IRW-texture ABI OT detection algorithm with and without the use of NWP tropopause temperature information relative to statistics for the WV-IRW BTD method.

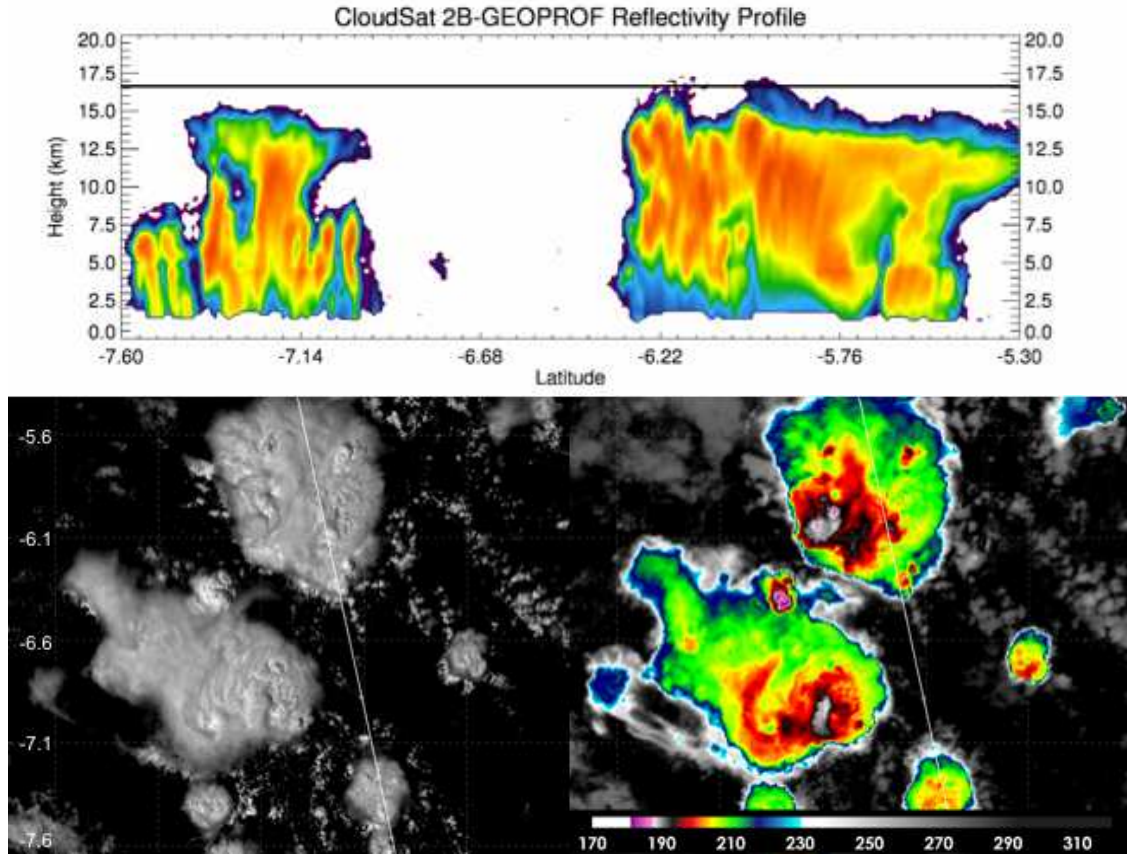


Figure 21 - (top) A CloudSat overpass of a deep convective cloud with an OT over the Congo on 29 November 2008 at 1213 UTC. The region within the two vertical dashed lines is the OT. The horizontal lines denote the peak height of the OT and the height of the anvil cloud surrounding the OT. (bottom-left) Contrast-enhanced Aqua MODIS 0.25 km visible channel imagery at 1210 UTC. (bottom-right) Aqua MODIS 1 km IRW BT imagery. The white diagonal line in the bottom panels shows the location of the CloudSat overpass from the top panel.

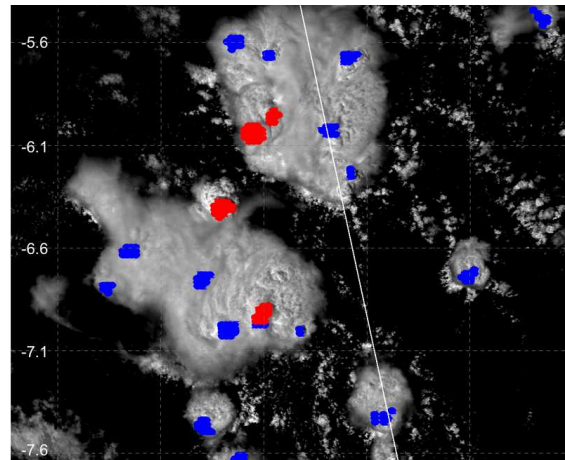


Figure 22 - IRW-texture OT detections with (red pixels) and without (blue pixels) the use of a GDAS tropopause temperature check for the case shown in Figure 20. The OTs detected with the tropopause temperature check were also detected when this check was removed.

4.3.2 ARW-based Synthetic ABI OT Detections and Comparison With ARW THMR Output

OTs identified within synthetic GOES-R ABI IRW and WV-IRW BTD imagery are compared with ARW THMR to provide a qualitative validation of these detection techniques. An example of synthetic IRW imagery, output from the two OT detection techniques, and “truth” OT locations defined by ARW THMR is shown in Figure 23 for the simulation time corresponding to 2340 UTC on 4 June 2005. Figure 23a shows several regions of convection across the domain, with a minimum IRW BT of ~195 K in northeast Oklahoma which is comparable to the cases shown in previous sections. ARW pixels with cloud tops above the tropopause (175 hPa) occupy much of the anvil cloud and those above the 165 hPa level are confined to regions with colder IRW BTs (see Fig. 23b). OT detections from the IRW-texture method show few false alarms and capture the two regions with high confidence OTs (see Fig. 23c). Truth OTs across Illinois are completely missed by this method. OT detections from the WV-IRW BTD are fewer than those from IRW-texture, but also capture both sets of high confidence pixels as well as portions of the storms in Illinois (see Fig. 23d).

The results of a quantitative comparison between the two OT detection techniques and truth OT locations are provided in Table 11. The results show that the BTD between the OT minimum BT and mean surrounding anvil BT can be used to improve the FAR of the IRW-texture technique. Depending upon the cloud-top height considered as overshooting, the FAR improves by ~12% to 19% when the required BT difference is increased from 6.5 to 10.5 K, but the total number of pixels that satisfy the more stringent criteria decreases by ~64%. Despite this substantial decrease, the percentage of high confidence pixels detected decreases by only ~3%, which indicates that a greater OT-anvil BTD corresponds with significant vertical hydrometeor flux and higher cloud tops. When the required OT-anvil BTD is reduced, the FAR for all overshooting pixels actually improves by ~1%, but increases significantly if significant overshooting pixels are considered. Table 11 also shows that the accuracy of the IRW-texture technique is ~15-17% better when 16 of the 16 possible surrounding anvil pixels are included in the mean. The percentage of high confidence OT pixels is identical for both the 5 of 16 and 16 of 16 pixel criteria (not shown), suggesting that the number of valid surrounding anvil pixels can also be used as a quality control parameter.

The difference between the WV-IRW BTD FAR when the truth OT height threshold is changed from 175 hPa to 165 hPa indicates that many of the BTD pixels correspond to an overshooting magnitude < 0.5 km. The FAR difference is not as pronounced for the IRW-texture technique. This result could be related to the findings of Schmetz et al. (1997), where they noted that the maximum WV-IRW BTD occurred with cloud tops just above the tropopause and that this BTD can decrease with greater overshooting magnitude. Though the FAR for the WV-IRW BTD is quite low for the 175 hPa truth OT threshold, the IRW-texture technique is comparable when the OT-anvil BTD is increased. For overshooting magnitudes > 0.5 km, all IRW-texture algorithm settings perform better than the 2 K WV-IRW BTD. The IRW-texture outperforms the 3 K WV-IRW BTD with an 8.5 K OT-anvil BTD.

The primary difference in validation results between the two techniques is shown through the percentage of identified high confidence pixels. For the qualitative comparisons shown in previous sections, a 3 K WV-IRW BTD is shown to be more reliable than a 2 K BTD. The detection rate for high confidence OTs decreases significantly when this BTD threshold is adjusted from 2 to 3 K, whereas the detection rate from the IRW-texture remains fairly constant when the OT-anvil BTD is adjusted. A maximum high confidence OT pixel detection rate of 34.8% for IRW-texture and 28% for WV-IRW BTD suggests that some aspects of these techniques are inhibiting high confidence pixel detection. The synthetic ABI imagery at the high confidence OT pixel locations is analyzed here to determine why these are not being detected at a higher rate by either technique. The results shown that the reason behind the WV-IRW high confidence pixel non-detection is straightforward in that 72% of these pixels had a WV-IRW BTD < 2 K.

For the IRW-texture technique, analysis indicates that all high confidence pixels have IRW BTs \leq 215 K (not shown). The IRW BT at the high confidence pixel location is \leq 6.5 K colder than the mean surrounding anvil for \sim 26% of all observations. \sim 9% of the high confidence pixels were not surrounded by at least 5 pixels with IRW BTD \leq 225 K, implying the presence of either a small or warm (i.e. $>$ 225 K) anvil cloud surrounding some high confidence pixels (not shown). \sim 22% of the high confidence pixels were within 15 km of another colder candidate overshooting pixel, so these too would be excluded from detection (not shown). The remaining 12% of high confidence pixels were left undetected because the IRW-texture method identifies pixels that are at least 50% colder than the surrounding anvil. The high confidence OT detection percentage would increase by \sim 8% to 43% if pixels 25% colder than the mean surrounding anvil BT were also considered OT pixels (not shown). This suggests that the high confidence OTs from ARW THMR may be of larger size than those evident in the synthetic IRW satellite imagery, possibly due to NWP effective model resolution and diffusion processes. In one study, the effective resolution has been determined to be 7 times the horizontal grid spacing, which would imply a 14 km effective resolution for the ARW simulation discussed here. (See <http://issuu.com/publishgold/docs/wrfarw> for details).

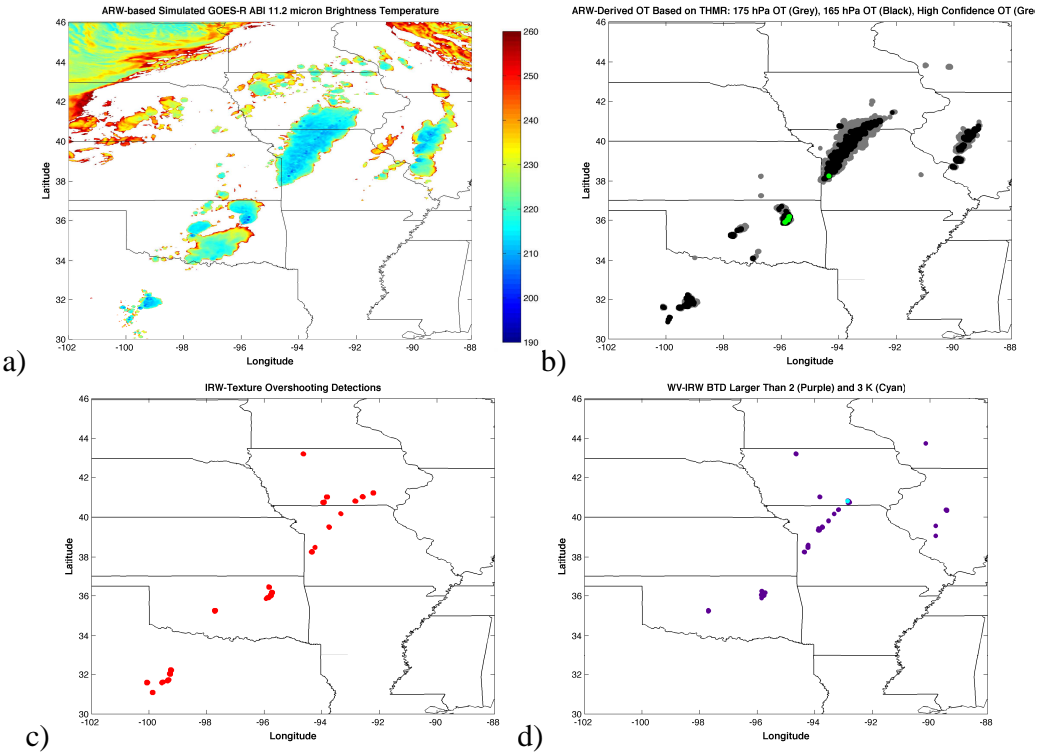


Figure 23 - a) Synthetic GOES-R ABI 11.2 μm IRW channel imagery. The color enhancement matches that shown in Fig. 9. **b)** Truth OT pixels as defined by ARW THMR. OT pixels with cloud tops above the 175 hPa level are colored in grey, pixels with tops above the 165 hPa level are colored in black, and high confidence OT pixels are colored in green. **c)** IRW-texture OT detections **d)** WV-IRW BTD values between 2 and 3 K (purple) and greater than 3 K (cyan). All images correspond to the 2340 UTC timestep on 4 June 2005 of the ARW simulation. The cluster of high confidence OTs in northeast Oklahoma corresponds to the clouds shown in Figure 1.

Overshooting Top Detection Method	False Alarm Rate < 175 hPa Cloud-Top 5 of 16 Pixels Included in Mean	False Alarm Rate < 165 hPa Cloud-Top 5 (16) of 16 Pixels Included in Mean	Percentage of Total High Confidence Pixels Identified	Number of Detected Pixels 5 (16) of 16 Pixels Included in Mean
IRW-Texture OT \geq 4.5 K Colder Than Surrounding Anvil	14.4%	43.7% (32.5%)	36.0%	4105 (2921)
IRW-Texture OT \geq 5.5 K Colder Than Surrounding Anvil	14.0%	40.9% (27.0%)	35.1%	3327 (2078)
IRW-Texture OT \geq 6.5 K Colder Than Surrounding Anvil	15.9%	38.8% (22.7%)	34.8%	2440 (1603)
IRW-Texture OT \geq 7.5 K Colder Than Surrounding Anvil	13.4%	35.2% (17.5%)	34.8%	1936 (1258)
IRW-Texture OT \geq 8.5 K Colder Than Surrounding Anvil	10.2%	31.2% (14.7%)	32.4%	1447 (908)
IRW-Texture OT \geq 9.5 K Colder Than Surrounding Anvil	7.9%	24.8% (8.6%)	32.4%	1145 (716)
IRW-Texture OT \geq 10.5 K Colder Than Surrounding Anvil	4.2%	19.6% (4.2%)	31.5%	884 (566)
WV-IRW BTD \geq 2 K	5.1%	46.1%	28.0%	1123
WV-IRW BTD \geq 3 K	2.3%	32.6%	1.5%	43

Table 11 - Results from a statistical comparison between OTs detected in synthetic ABI IRW channel imagery, WV-IRW BT difference imagery, and truth OT locations defined by ARW THMR. Results for the baseline ABI OT detection algorithm settings are highlighted in bold text.

4.3.3 MODIS + AVHRR Enhanced-V and ATC Database

55 MODIS and AVHRR images with enhanced-V signatures have been processed within the ABI enhanced-V ATC detection algorithm. Figure 24 provides an example of OT and ATC detections for a case on 7 April 2006. Four of the five ATCs present in this image are detected by the ABI algorithm. Only OTs associated with an ATC are displayed for this example. In reality, the number of OT detections significantly outnumbers ATC detections. Figure 25 provides an example of this in the vicinity of four individual enhanced-V producing storms. OT detections are scattered about the four images, but ATCs are only detected for storms with a clear enhanced-V signature.

Table 12 shows the validation results when the ABI algorithm is applied to all 55 cases with 203 enhanced-V producing storms. The 24 % FAR meets the enhanced-V signature detection algorithm accuracy requirement of 25% maximum FAR specified in the F&PS document. 62 % of the enhanced-V producing storms in our database (126 of 203 storms) were accurately detected. Since the primary application of this algorithm would be severe weather forecasting, we also determined how often the detected enhanced-V ATC storms produced severe weather. Analysis indicates that 72% of the 203 enhanced-V ATC storms produced severe weather. Table 12 shows that 76% of storms with detected ATCs produced severe weather within +/- 30 mins and 60 km of the OT location. 66% of the undetected enhanced-V ATC storms produced severe weather. These results indicate that the ABI enhanced-V algorithm is detecting a higher than average percentage of severe storms and will likely be useful for severe weather forecasting in the GOES-R era.

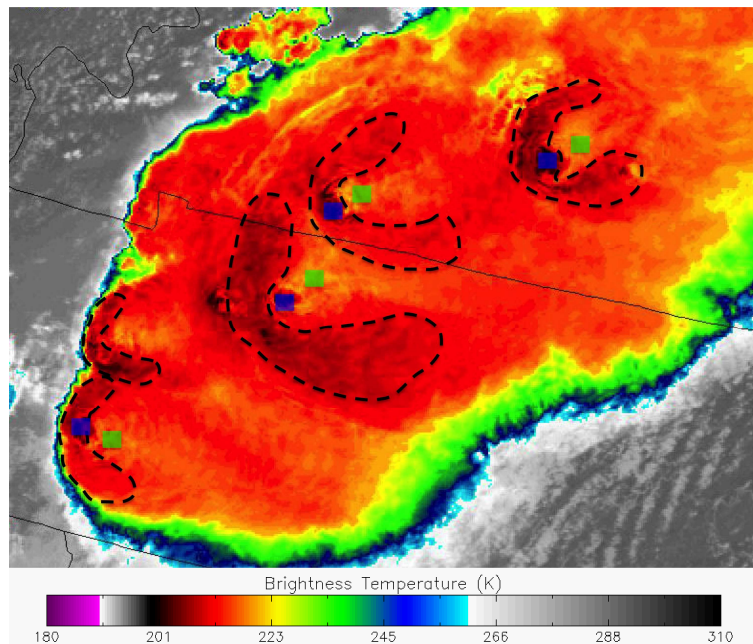


Figure 24 - Enhanced-V ATC detections with color-enhanced proxy GOES-R ABI IR window channel imagery at 1845 UTC on 7 April 2006. Enhanced-V locations are outlined in black dashed lines. Blue symbols are OT detects and green symbols are associated downstream warm regions, which together form the ATC. Only OTs with ATCs are shown.

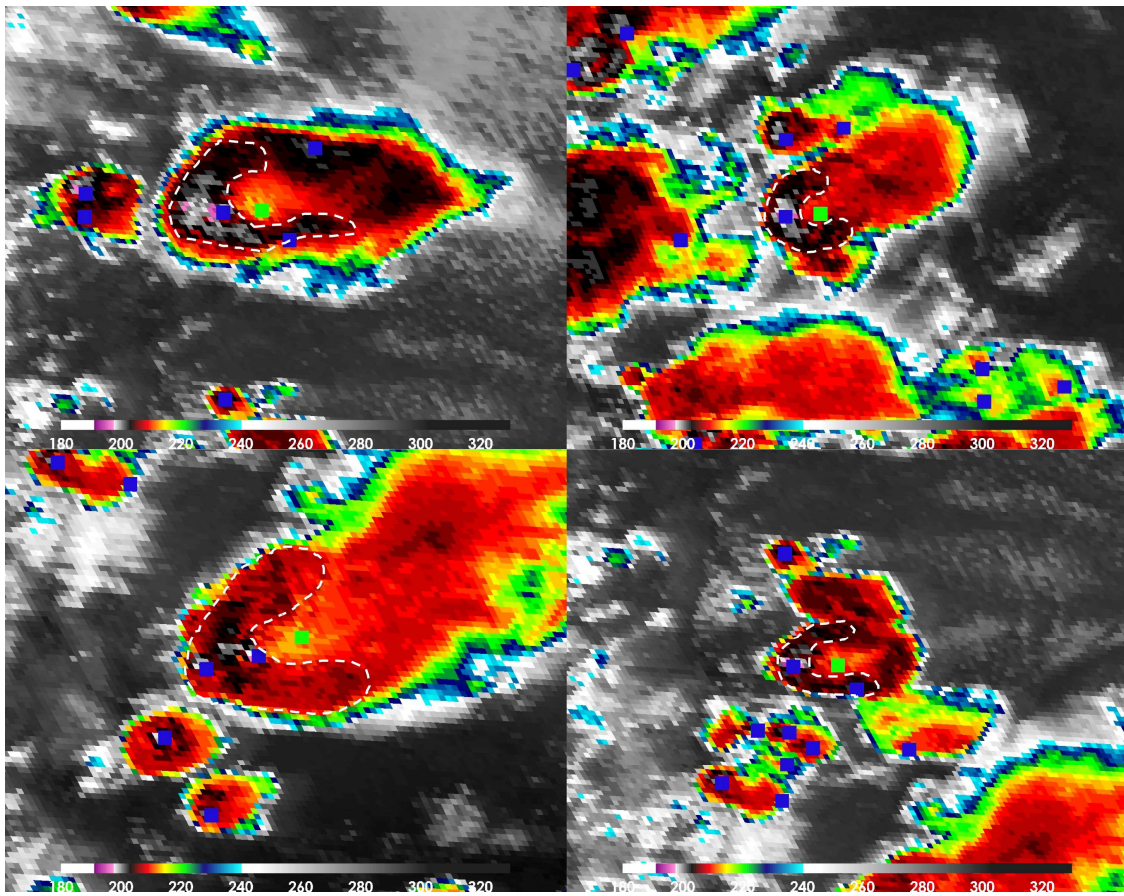


Figure 25 – A gallery of four enhanced-V producing storms in AVHRR-based proxy ABI 10.8 μ m IRW imagery with OT and ATC detection output. The case occurred on 10 May 2004 at 2315 UTC. Blue (Green) squares show OT (ATC) detections and the white dashed line highlights the location of the enhanced-V signature in each panel.

Input Imagery to ABI Enhanced-V ATC Detection	False Alarm Ratio (FAR)	Probability of Detection (POD)	% of Accurately Detected Enhanced-V ATCs with Severe Weather within +/- 30 minutes and 60 km of the OT location
Proxy ABI From MODIS and AVHRR	24 %	62 %	76 %

Table 12 - Validation statistics for the ABI enhanced-V ATC detection algorithm.

5 PRACTICAL CONSIDERATIONS

5.1 Numerical Computation Considerations

The OT and ATC algorithms are implemented sequentially, where the ATC algorithm depends upon OT output. If no OT is detected for a given storm, an enhanced-V ATC cannot be detected even if one were present in the image. As stated above, NWP tropopause information is required by the OT algorithm to improve OT detection accuracy. The OT algorithm currently uses 6-hr forecasts within the FRAMEWORK. However, if these are not available, we feel that any forecast time interval up to 24 hours can be utilized.

5.2 Programming and Procedural Considerations

The OT and ATC algorithms are pixel-by-pixel algorithms that take into account spatial cloud temperature information. Therefore a border around the periphery of the image will always be present where no OT or ATC are detected. The algorithm also assumes that extra scanlines will be read in within each FRAMEWORK image segment. If no extra lines are read in, each image segment will have a border in which the OT and ATC algorithms cannot operate.

5.3 Quality Assessment and Diagnostics

Since no database of all CONUS OT and enhanced-V events currently exists or will exist in the future, it will be very challenging to evaluate these algorithms in a quantitative manner in real-time. It is unlikely that the CloudSat and CALIPSO instruments will still be operating in the GOES-R era due to their age, so one will have to develop a means to objectively identify OT events using a cloud profiling instrument that is operating at this future time. One will also have to subjectively analyze ABI IRW imagery to develop a list of storms with the enhanced-V signature.

5.4 Exception Handling

The OT and enhanced-V ATC algorithms include checking the validity of each ABI channel 14 pixel before processing. These algorithms also expect the main processing framework to flag any pixels with missing geolocation or viewing geometry information.

5.5 Algorithm Validation

See section 5.3 above

6 ASSUMPTIONS AND LIMITATIONS

The following sections describe the current limitations and assumptions in the current version of the OT and enhanced-V ATC detection algorithms.

6.1 Performance

The following assumptions have been made in developing and estimating the performance of the OT and enhanced-V ATC algorithms. The following lists contain the current assumptions and proposed mitigation strategies in parentheses.

1. NWP data of comparable or superior quality to the current 6 hourly GFS forecasts are available. (Use longer range GFS forecasts or switch to another NWP source –WRF, NAM).
2. The input NWP model accurately represents the tropopause temperature. (If NWP is consistently errant or biased, use different NWP model data)
3. The processing system allows for processing of multiple pixels at once such that the algorithms can derive spatial texture and BT pattern information. (No mitigation possible)

6.2 Assumed Sensor Performance

It is assumed that the ABI sensor will meet its current specifications. However, the OT and enhanced-V ATC algorithms will be affected if the ABI 11.2 μm IRW channel 14 does not collect high-quality observations since these algorithms only use data from this single channel. The developers assume that the ABI 10.4 μm channel 13 can be used in the event that channel 14 is unavailable.

6.3 Pre-Planned Product Improvements

While development of the baseline OT and enhanced-V ATC algorithms continue, we expect in the coming years to focus on the following issues.

6.3.1 Improved OT Detection In Banded Cold Cirrus Cloud Cases

The OT algorithm has produced false detections in events with highly textured cold cirrus clouds. These clouds can have IRW BTs that are both colder than the NWP tropopause and 215 K and meet the OT-anvil BT difference criterion. We plan to look at these cases in detail and will develop a method for mitigating false detection.

6.3.2 Inclusion of NWP 250 hPa Wind Direction

The downstream warm region in an ATC is located downwind of the OT. In order to improve ATC algorithm FAR, we plan to include the 250 hPa wind direction to confine the 25x50 km ATC search region. The search region will be restricted to +/- 45 deg of the 250 hPa wind direction. Preliminary testing shows that use of this wind field produces a ~8% improvement in FAR for the cases examined in Table 12.

7 REFERENCES

- Ackerman, S.A., 1996: Global satellite observations of negative brightness temperature differences between 11 and 6.7 μm . *J. Atmos. Sci.*, **53**, 2803–2812.
- Adler, R.F., and R.A. Mack, 1986: Thunderstorm cloud top dynamics as inferred from satellite observations and a cloud top parcel model. *J. Atmos. Sci.*, **43**, 1945–1960.
- Bedka, K. M., 2010: Overshooting cloud top detections using MSG SEVIRI infrared brightness temperatures and their relationship to severe weather over Europe. Accepted to *Atmos. Res.*, September 2010.
- Bedka, K. M., J. Brunner, R. Dworak, W. Feltz, J. Otkin, and T. Greenwald, 2010: Objective satellite-based overshooting top detection using infrared window channel brightness temperature gradients. *J. Appl. Meteor. And Climatol.*, **49**, 181-202.
- Berendes, T. A., J. R. Mecikalski, W. M. MacKenzie, Jr., K. M. Bedka, and U. S. Nair, 2008: Convective cloud identification and classification in daytime satellite imagery using standard deviation limited adaptive clustering, *J. Geophys. Res.*, **113**, D20207, doi:10.1029/2008JD010287.
- Brunner, J. C., S. A. Ackerman, A. S. Bachmeier, and R. M. Rabin, 2007: A Quantitative Analysis of the enhanced-V feature in relation to severe weather. *Wea. Forecasting*, **22**, 853–872.
- CloudSat Standard Data Products Handbook. Available online at:
http://www.cloudsat.cira.colostate.edu/cloudsat_documentation/CloudSat_Data_Users_Handbook.pdf
- Fritz, S., and I. Laszlo, 1993: Detection of water vapor in the stratosphere over very high clouds in the tropics, *J. Geophys. Res.*, **98**, 22959-22967.
- GOES-R Series Ground Segment (GS) Project Functional and Performance Specification (F&PS) [G417-R-FPS-0089]
- GOES-R Acronym and Glossary (P417-R-LIST-0142)
- Heymsfield, G.M., G. Szejwach, S. Schotz, and R.H. Blackmer, 1983: Upper-level structure of Oklahoma tornadic storms on 2 May 1979. II: Proposed explanation of “V” pattern and internal warm region in infrared observations. *J. Atmos. Sci.*, **40**, 1756–1767.
- Heymsfield G. M., L. Tian, A. J. Heymsfield, L. Li, and S. Guimond, 2010: Characteristics of deep tropical and sub-tropical convection from nadir-viewing high-altitude airborne doppler radar. *J. Atmos. Sci.*, In Press.

Mace, G. G., R. Marchand and G. L. Stephens, 2007: Global hydrometeor occurrence as observed by CloudSat; Initial observations from summer 2006, *Geophys. Res. Lett.*, Vol. **34**, L09808, doi:10.1029/2006GL029017.

McCann, D.W., 1983: The enhanced-V: A satellite observable severe storm signature. *Mon. Wea. Rev.*, **111**, 887–894.

Mosher, F. R., 2001. A satellite diagnostic of global convection. *Preprints, 11th Conference on Satellite Meteorology and Oceanography*, Madison, WI. Amer. Meteor. Soc. 416-419.

Negri, A. J., 1982: Cloud-top structure of tornadic storms on 10 April 1979 from rapid scan and stereo satellite observations. *Bull. Amer. Meteor. Soc.*, **63**, 1151-1159.

Otkin, J. A., T. J. Greenwald, J. Sieglaff, and H.-L. Huang, 2009: Validation of a large-scale simulated brightness temperature dataset using SEVIRI satellite observations. *J. Appl. Meteor. And Climatol.*, **48**, 1613-1626.

Schmetz, J., S. A. Tjemkes, M. Gube, and L. van de Berg, 1997: Monitoring deep convection and convective overshooting with METEOSAT. *Adv. Space. Res.*, **19**, 433-441.

Setvak, M, R. M. Rabin, P. K. Wang, 2007: Contribution of the MODIS instrument to observations of deep convective storms and stratospheric moisture detection in GOES and MSG imagery. *Atmos. Res.*, **83**, 505-518.

Skamarock, W. C., J. B. Klemp, J. Dudhia, D. O. Gill, D. M. Barker, W. Wang, and J. G. Powers, 2005: A description of the Advanced Research WRF Version 2. NCAR Tech. Note/TN-468+STR, 88 pp.

Stephens, G.L., D.G. Vane, R.J. Boain, G.G. Mace, K. Sassen, Z. Wang, A.J. Illingworth, E.J. O'Connor, W.B. Rossow, S.L. Durden, S.D. Miller, R.T. Austin, A. Benedetti, C. Mitrescu, and the CloudSat Science Team, 2002: The CloudSat mission and the A-Train. *Bull. Amer. Meteor. Soc.*, **83**, 1771–1790.

Wang, P.K., 2003. Moisture plumes above thunderstorm anvils and their contribution to cross-tropopause transport of water vapor in midlatitudes. *J. Geophys. Res.* **108** (D6), AAC 51–AAC 515.